Non-muscle myosin II regulates presynaptic actin assemblies and neuronal mechanobiology

Biljana Ermanoska[1,§]* and Avital A. Rodal[1]*

[1] Department of Biology, Brandeis University, Waltham, MA
[§] Current affiliation: University of Antwerp, Faculty of Medicine and Health Sciences, Antwerp, Belgium
[*] Corresponding authors:
Email: biljana.ermanoska@gmail.com, arodal@brandeis.edu

Abstract

Neuromuscular junctions (NMJs) are evolutionarily ancient, specialized contacts between neurons and muscles. Axons and NMJs must endure mechanical strain through a lifetime of muscle contraction, making them vulnerable to aging and neurodegenerative conditions. However, cellular strategies for mitigating this mechanical stress remain unknown. In this study, we used *Drosophila* larval NMJs to investigate the role of actin and myosin (actomyosin)-mediated contractility in generating and responding to cellular forces at the neuron-muscle interface. We identified a new long-lived, low-turnover presynaptic actin core traversing the NMJ, which partly co-localizes with non-muscle myosin II (NMII). Neuronal RNAi of NMII induced disorganization of this core, suggesting that this structure might have contractile properties. Interestingly, neuronal RNAi of NMII also decreased NMII levels in the postsynaptic muscle proximal to neurons, suggesting that neuronal actomyosin rearrangements propagate their effects trans-synaptically. We also observed reduced Integrin levels upon NMII knockdown, indicating that neuronal actomyosin disruption triggers rearrangements of Integrin-mediated connections between neurons and surrounding muscle tissue. In summary, our study identifies a previously uncharacterized presynaptic actomyosin subpopulation that upholds the neuronal mechanical continuum, transmits signals to adjacent muscle tissue, and collaborates with Integrin receptors to govern the mechanobiology of the neuromuscular junction.

Keywords: *Drosophila*, neuromuscular junction, actin cytoskeleton, non-muscle myosin II, integrin, mechanobiology

Introduction

Neuromuscular junctions (NMJs) and axons must weather continuous mechanical strain from muscle contractions, while also maintaining contact with the significantly more rigid muscle tissue[1]. Thus, the NMJ offers an excellent tissue mechanics model to study evolutionary conserved mechanisms by which "soft" neurons sustain their shape, function and plasticity while facing substantial mechanical challenges. NMJs are susceptible to aging and neurodegenerative disorders, and retraction of synaptic terminals precedes the degeneration of axons and subsequent loss of neuronal cell bodies in many diseases[2]. Therefore, understanding how mechanical forces are sensed, generated, and transmitted within neurons and between neurons and their surrounding muscle is an important and understudied topic.

The actin cytoskeleton underlies multiple conserved mechanisms by which cells generate and respond to cellular forces[3]. For example, endocytosis is supported by submicron-sized (~200 nm), short-lived (<30s) force-generating actin patches, predominantly containing Arp2/3-nucleated branched filamentous actin (F-actin)[4, 5]. On the other hand, cell and tissue-scale forces are often mediated by the actin-based motor non-muscle Myosin II (NMII)[6]. Contraction-competent NMII self-assembles into bipolar filaments, with motor domains at both ends that are capable of binding antiparallel actin filaments. In this way, NMII induces sliding of the filaments, resulting in the generation of contractile forces for a variety of cellular needs[7,8]. As one example, ventral stress fibers are micron-sized, long-lived assemblies of linear F-actin that recruit NMII and play a key role in cellular mechanics and force sensing in cultured cells[9]. Thus, depending on the specific force requirements, actin assemblies with variable sizes, lifetime, and molecular composition support different cellular processes.

Numerous actin-based and myosin-associated structures have been observed in axons and presynaptic terminals and could play important roles in the mechanical properties of neurons. An axonal submembranous cytoskeleton (SMC), composed of periodic repeats of spectrin, actin rings and non-muscle myosin II, was described in the past decade[10-12]. This structure is conserved in mammalian and invertebrate neurons[13], and supports periodic organization of numerous other molecules important for neurotransmission, cell adhesion and molecular transport[14]. A subset of the SMC represents radial actomyosin, which specifically regulates axonal diameter, conduction, and the passage of larger cargos[12, 15]. Another population of axonal myosin shows a more longitudinal distribution[16]; however it remains unknown if these longitudinal structures bridge neighboring actin rings, associate with other axonal actin assemblies such as trails[17], or have yet another function. SMC periodicity diminishes at synaptic boutons, where actin is found in mesh-like assemblies at the active zone, rails between the active zone and deeper reserve pools, and corrals around the whole presynaptic compartment[18], as well as in transient puncta with features of endocytic events[5]. Currently it is unknown if any of these assemblies recruit NMII, or how they contribute to the mechanical properties of presynaptic terminals.

Functional studies also implicate actomyosin structures in NMJ physiology. At the *Drosophila* larval NMJ, depletion of neuronal NMII disrupts the organization of synaptic vesicles[19], suggesting this motor might associate with at least fraction of presynaptic actin structures. In line with these findings, at the *Drosophila* embryonic NMJ, changing mechanical tension can modulate synaptic vesicle organization and synaptic plasticity[20]. Moreover, neuronal depletion of *Drosophila* NMII at the larval NMJ promotes formation of nascent boutons by blebbing[21]. These structures depend on neuronal activity as well as muscle contraction[21-23], and can sometimes mature into functional boutons[21, 22, 24], representing a form of activity-dependent structural plasticity. Thus, NMII, and by extension actomyosin contractility, are necessary to maintain the integrity of boutons experiencing muscle contractions and

to regulate the growth of new synaptic arbors. Taken together, these findings highlight the ability of the NMJ to respond to mechanical forces. However, the subcellular organization and functions of the presynaptic actomyosin assemblies that underlie these events remain largely unknown.

Actomyosin assemblies coordinate with additional multi-protein machineries to control cellular mechanosensing and mechanotransduction. For example, ventral stress fibers are physically coupled to focal adhesion complexes[9] along the ventral membrane of adherent cells. At the center of focal adhesion-mediated intra- and extracellular force-tuning are a set of metazoan Integrin receptors that bridge cytoplasmic cytoskeletal components to a large variety of extracellular matrix (ECM) molecules and counter-receptors on other cell types[25]. In this way, via biochemical and mechanical activation of Integrins, cells sense the mechanical features of their surroundings and transduce these forces into biological signals by inducing regulated assembly and maturation of focal adhesions. The crucial role Integrins play in synaptic biology has been well established in vertebrates[26] and at the *Drosophila* NMJ, where their disruption[27, 28] or targeting their interactors (components of the ECM[29, 30], enzymes involved in ECM glycosylation[31], an Integrin activator[32], or the cytoskeletal linker Talin[28]), induce a range of morphological defects and affect activity-dependent synaptic plasticity. These studies highlight the importance of Integrins in neuronal function and position these molecules as likely candidates to control transsynaptic neuron-to-muscle communication and NMJ mechanobiology.

In this study, we examined presynaptic actin assemblies at the *Drosophila* larval NMJ. and identified a long-lived, low turnover linear actin core traversing the axon terminal. NMII regulates the organization of this core, suggesting that these are actomyosin structures, likely with contractile properties. Strikingly, neuronal depletion of NMII induced decrease of NMII levels in the postsynaptic muscle proximal to boutons, suggesting that neuronal actomyosin rearrangements can propagate their effects transsynaptically. Next, we considered Integrin receptors as mediators of the transsynaptic NMII changes and found a decrease in Integrin foci both pre- and postsynaptically, indicating that neuronal actomyosin defects sensed via local Integrin receptors can propagate to the surrounding muscle tissue. In sum, we demonstrate that a previously unrecognized subpopulation of presynaptic actomyosin maintains the mechanical continuum from neuron to muscle, and thus regulates the mechanobiology of the neuromuscular junction.

Results

Discrete presynaptic actin assemblies at the Drosophila NMJ

At the *Drosophila* larval NMJ, presynaptic terminals innervate the mechanically active postsynaptic muscle, making this synapse an ideal model to study biological solutions to mechanical challenges at the neuron-muscle interface (**Fig. 1A**). In a previous study, we demonstrated that a subpopulation of patch-like, submicron sized, presynaptic actin is amenable to live imaging via confocal microscopy and subsequent quantitative analysis[5]. To improve the visualization of these small and transient actin structures, we re-designed a broadly used, genetically encoded F-actin marker GMA (GFP Moesin Actin-binding domain)[5, 33], by tagging it with the bright mNeonGreen[34] fluorescent protein (mNGMA). To assess the structure and function of presynaptic actin we generated QF-driven, QUAS-mNGMA (QmNGMA) transgenes. This allowed us to genetically combine two binary expression systems (UAS/Gal4 and QUAS/QF[35, 36]) in a single fly and to visualize presynaptic actin, while independently manipulating different actin-associated proteins via RNAi. Finally, to improve the resolution of the presynaptic actin structures of interest, we used Airyscan microscopy.

With these tools in hand, we imaged presynaptic actin in live dissected larvae with intact brains and axons. Interestingly, along with numerous spot-like F-actin assemblies throughout the NMJ, the improved signal-to-noise and resolution provided by our approach also revealed a previously unrecognized linear, cable-like actin structure traversing the NMJ (**Fig. 1B**, **Supp. Movie S1**). To enable unbiased analysis of these structures we built a WEKA machine learning-based classifier[37] in the image analysis software FIJI[38] that allowed us to specifically segment round from linear F-actin structures at the NMJ (**Fig. 1B**, **Fig. S1**). Next, we verified the existence of the linear actin core with the broadly used F-actin marker, Lifeact[39], tagged with the Halo self-labeling protein tag (*UAS-Lifeact::Halo*). Neuronally expressed Lifeact::Halo (*C155-Gal4>Lifeact::Halo*) labeled the linear actin core as well as the previously observed spot-like structures at the NMJ (**Fig. 1C**). Thus, we confirmed that the newly identified linear actin assemblies can be visualized with at least two independent, bright actin markers in live larval preparations.

In the course of our live imaging, we noticed that the presynaptic actin core is stable (in space and time) over minutes (**Fig. S2A**), unlike the transient, spot-like structures, which have lifetimes in the tens of seconds and likely represent endocytic events[5] (**Fig. S2B**). In addition, fluorescent recovery after photobleaching (FRAP) of the QmNGMA marker demonstrated an immediate relabeling of the same, practically unchanged presynaptic actin core structure, further supporting the idea that these are long-lived assemblies on which the F-actin marker can readily bind and unbind (**Fig. S2C-D**). To explore the dynamics of actin directly, we generated a QUAS transgene carrying the Actin5C *Drosophila* isoform, tagged with the bright, red fluorescent protein mScarlet-I[40] (QAct5C::mScarI). Live imaging of QAct5C::mScarI showed that tagged actin integrated into spot-like and linear F-actin structures along the core, albeit less continuous compared to QmNGMA (**Fig. 1D**, **Fig. S2E**). FRAP analysis of QAct5C::mScarI demonstrated that the F-actin assemblies constituting the presynaptic actin core have slow but detectable recovery (**Fig. 1E-F**), suggesting that they do not turn over quickly. To independently test dynamics, we evaluated the sensitivity of the linear actin core to treatment with the actin-sequestering drug Latrunculin A/LatA. Incubation of dissected larvae for 30 minutes in 1 µM LatA led to the disappearance of distinct actin structures at the NMJ, including the core, while incubation with the DMSO solvent alone did not lead to loss of actin structures (**Fig. S2F-G**). These results indicate that the core does undergo dynamic turnover. In sum, we identified different presynaptic actin assemblies that vary in size and lifetime and are probably involved in distinct functions at synaptic terminals.

Molecular composition of the presynaptic actin core

A large number of actin-associated proteins define the assembly, shape, and stability of actin structures[41]. For example, actin nucleators such as the Arp2/3 complex and formins facilitate the generation of branched and linear actin filaments, respectively. Previously, we demonstrated that most of the endocytic actin patches at the NMJ co-localize with components of the Arp2/3 actin filament nucleation complex[5]. On the other hand, pharmacological inhibition of formins disrupted presynaptic protein composition, vesicle cycling, and endocytosis in induced synapses and hippocampal neurons[18, 42]. Thus, these studies suggest that distinct actin subpopulations supporting synaptic processes might be generated via different F-actin nucleators. We assessed the presence of nucleation machinery along the presynaptic actin core by imaging NMJs in larvae co-expressing Lifeact::Halo (to label F-actin) and GFP-tagged Arp3 or the formin Dia. We observed that a fraction of both Arp3::GFP (**Fig. 2A**; **Supp. Movie S2**) and Dia::GFP (**Fig. 2B**; **Supp. Movie S3**) punctate signal were visible along the linear actin core, unlike the diffuse

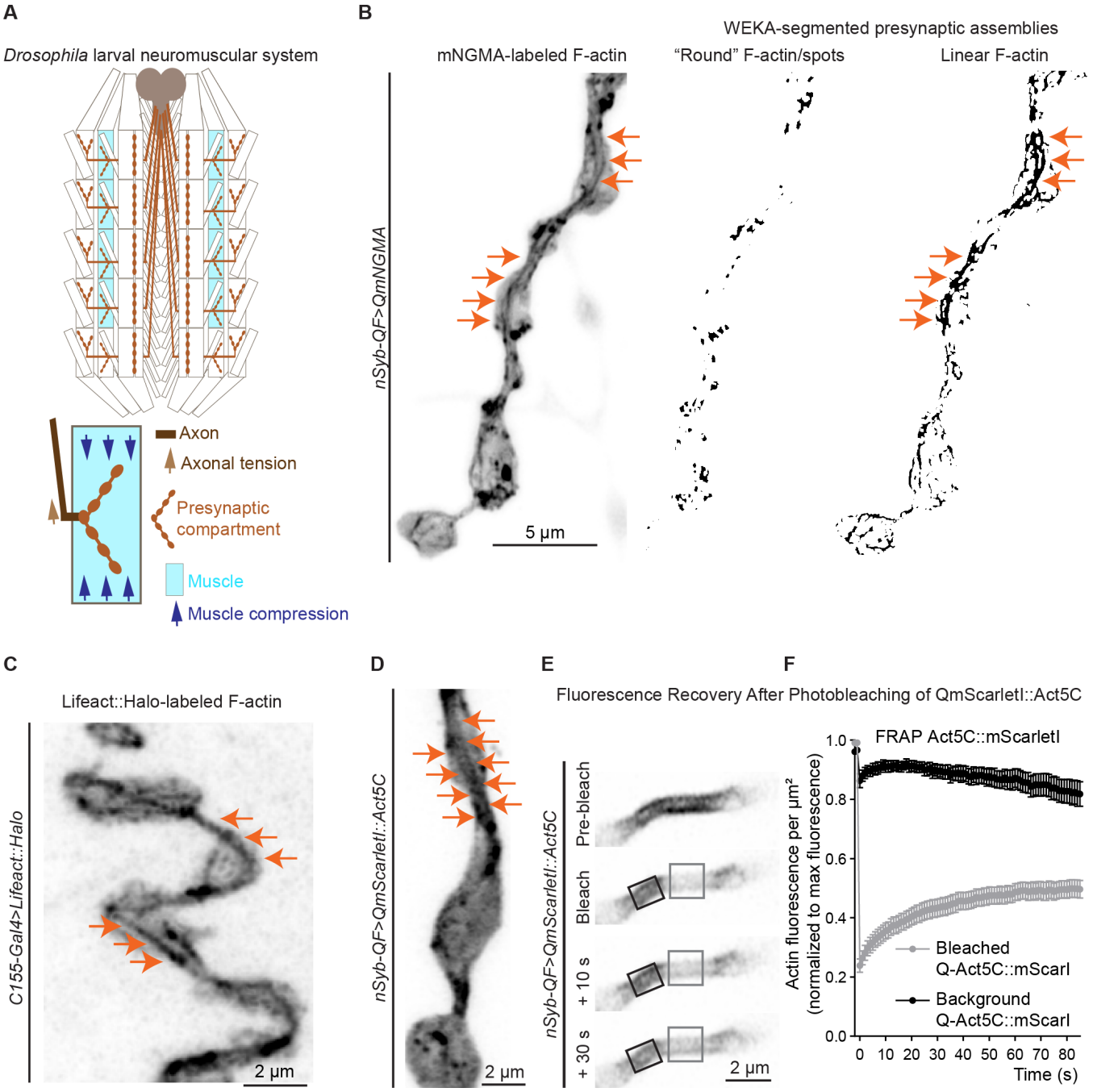

Fig. 1. Presynaptic actin cytoskeleton at the *Drosophila* larval NMJ. A) Diagram of the *Drosophila* larval neuromuscular system as a tissue mechanics model. The NMJ at muscle 4 (light blue) was predominantly assessed in this study. The presynaptic compartment (light brown) is subject to multiple mechanical forces including axonal tension (brown arrow) and compression due to muscle contractions (blue arrows). **B**) A single frame from live imaging of presynaptic actin assemblies visualized via neuronal expression of the genetically encoded actin marker mNeonGreen-GMA (mNGMA) in larval preparations with intact brains (see also **Supp. Movie S1**). WEKA segmentation was used to distinguish different actin subpopulations (round (spot-like), and linear, (cable-like or core) F-actin structures) and to facilitate their subsequent quantitative analysis. Orange arrows indicate a portion of the newly identified linear actin core traversing the NMJ. **C**) A single frame from live imaging of NMJs expressing an independent genetically encoded actin marker Lifeact::Halo delineates similar spot-like and cable-like (core) actin assemblies. Orange arrows indicate a portion of linear actin core. **D**) A single frame from live imaging of the *Drosophila* actin isoform 5C, tagged with the red fluorescent protein mScarlet-I (QAct5C::mScarI), similarly delineates the actin core in addition to round F-actin assemblies. **E**) Image sequence of FRAP of QAct5C::mScarI-labeled actin core. **F**) FRAP curve of QAct5C::mScarI (N = 16 NMJs, error bars represent SEM). Scale bars – 5 µm in A, 2 µm in other images. **See Table 1 for detailed genotypes.**

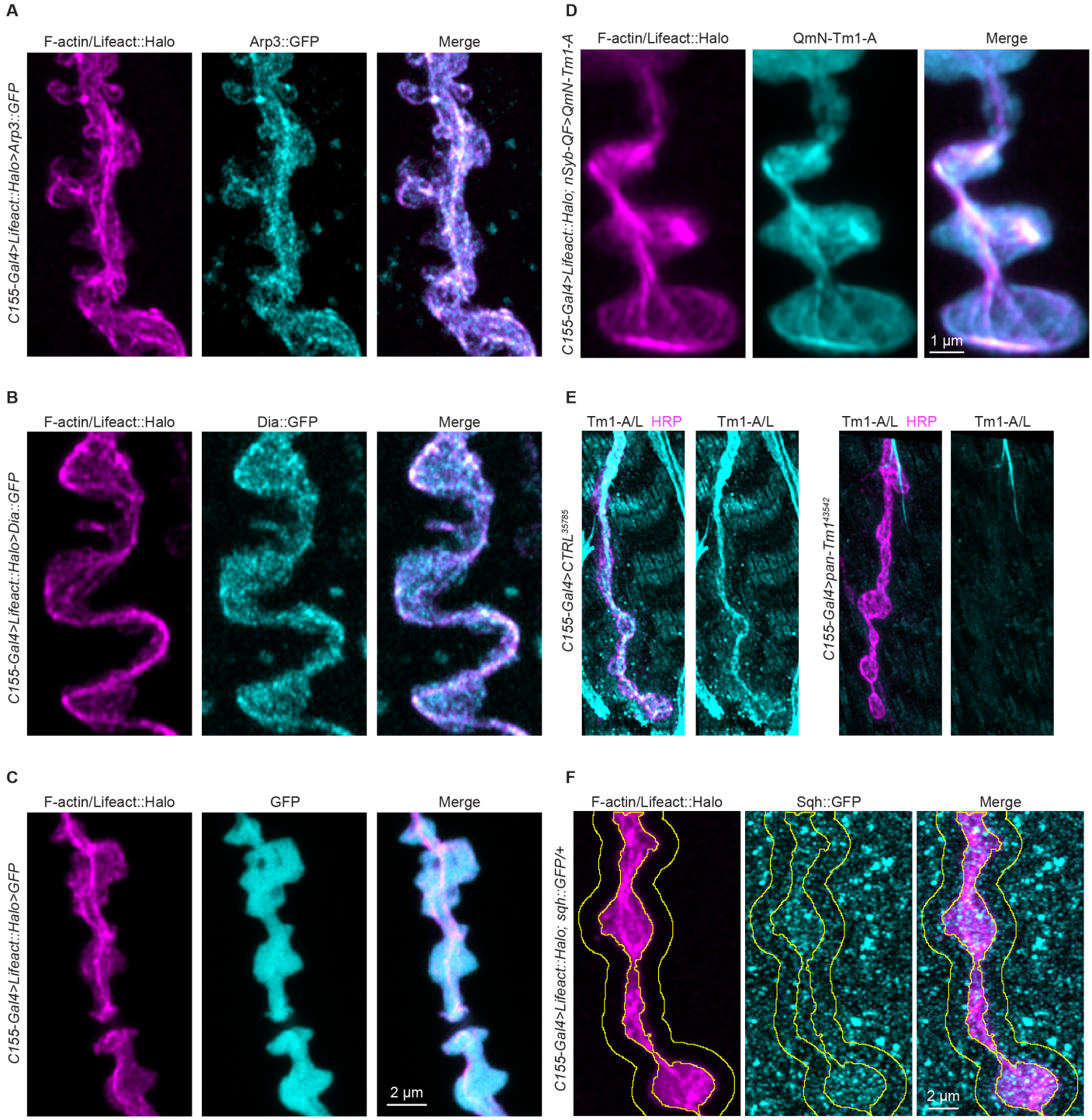

Fig. 2. Molecular composition of linear F-actin structures at the presynaptic core. A) Live imaging of the branched actin nucleator Arp2/3, visualized via Arp3::GFP (cyan), decorates spot-like and linear F-actin assemblies labeled with Lifeact::Halo (magenta). See also **Supp. Movie S2**. **B**) The linear actin nucleator formin/Dia::GFP (cyan) decorates actin cables (magenta), in addition to its punctate distribution throughout the NMJ (see also **Supp. Movie S3**). **C**) Diffuse cytosolic GFP (cyan) shows no specific enrichment or co-localization with presynaptic actin assemblies (magenta). See also **Supp. Movie S4**. **D**) The F-actin stabilizer Tm1-A is enriched in the linear Lifeact::Halo-marked actin assemblies along the presynaptic core. **E**) Endogenous Tm1 (cyan), detected via immunofluorescence, traverses the NMJ (labeled with HRP - magenta) in larvae expressing control RNAi in all neurons. The Tm1 signal is significantly decreased at NMJs of animals neuronally expressing a Tm1 RNAi line (*panTm1*^{43542}). See **Fig. S2H** for quantification. **F**) Distribution of the non-muscle myosin II light chain subunit sqh::GFP at the NMJ in live larvae expressing Lifeact::Halo in neurons. See also **Supp. Movie S5**. Scale bars in **C)** and **E**) – 2 µm; in **D**) – 1 µm. **See Table 1 for detailed genotypes.**

distribution of control cytosolic GFP (**Fig. 2C**; **Supp. Movie S4**). However, this fraction was relatively low, and co-localization analysis of these signals did not reveal different Pearson's R correlation (PCC) when compared to cytosolic GFP (**Fig. S3A**).

To further evaluate the molecular composition of the linear presynaptic actin structures, we investigated the localization of non-muscle Tropomyosins. Tropomyosins are important F-actin stabilizers, and co-polymerize with actin in linear structures such as yeast actin cables[43] and stress fibers in cultured mammalian cells[44]. The Tpm3.1 isoform is an integral part of the periodic axonal cytoskeleton, and neuronal morphology and function have been shown to depend on numerous tropomyosins[45, 46]. To ask if *Drosophila* non-muscle Tropomyosin 1/Tm1 associates with the linear presynaptic actin core, we generated transgenic flies containing QUAS-driven, mNeonGreen-tagged versions of two of the 18 predicted *Drosophila* Tm1 isoforms (QmN-Tm1-A and QmN-Tm1-L, respectively). When expressed in neurons (*nSyb-QF*) and imaged live, both QTm1 isoforms labeled linear structures traversing the NMJ (**Fig. S3B-C**). Q-Tm1-A had significant overlap with the actin marker Lifeact::Halo along the actin core, unlike the control cytosolic GFP (**Fig. 2D**). This was also quantified as a significantly higher Pearson's R values between Tm1-A and Lifeact, compared to cytosolic GFP vs Lifeact (**Fig. S3D**). In addition, the Q-Tm1-L signal was sensitive to the same LatA treatment that depolymerized all Q-mNGMA-labeled actin subpopulations (**Fig. S3E-F**), consistent with Tm1 association with the F-actin core. Finally, we performed immunostaining with an antibody that recognizes Tm1-A and Tm1-L[47], and observed a distribution resembling the presynaptic actin core in control animals (**Fig. 2E**). However, the antibody-detected Tm1 signal was strongly decreased at NMJs of larvae expressing RNAi targeting all Tm1 isoforms (*panTm1*^{43542}, **Fig. 2E**), or an independent line targeting Tm1-A (*Tm1*^{56869}, **Fig. S3G-H**), confirming the specificity of this signal. Importantly, this result suggests that the core is an endogenous structure and does not depend on expression of an F-actin marker. In sum, the linear presynaptic actin core is decorated by the F-actin stabilizer Tropomyosin, giving this structure a molecular signature resembling stress fibers[44].

Ventral stress fibers are actomyosin structures that sense and coordinate the adhesion of cultured cells to their substrates[9]. We were curious to learn if the linear presynaptic actin core would similarly recruit NMII. The mammalian NMII bipolar filament is composed from a complex of two heavy chains (HCs), two essential light chains (LCs) and two regulatory light chains (RLCs). The *Drosophila* NMII heavy chain is encoded by Zipper/Zip, and the light chain is encoded by Spaghetti squash/Sqh. To visualize NMII at the *Drosophila* NMJ, we used a well-established GFP-tagged spaghetti squash/Sqh::GFP transgene, expressed from its own promoter[48]. Using two independent *UAS-RNAi* lines targeting Sqh (*Sqh*^{32439} and *Sqh*^{33892}) and Zip (*Zip*^{65947} and *Zip*^{36727}) (**Fig. S4A-D**), we demonstrated that Sqh::GFP levels decrease upon neuronal depletion of either NMII subunit. Thus, we further used this tool as a readout of NMII localization at the NMJ. In live larvae expressing Sqh::GFP under its own promoter, together with neuronally driven Lifeact::Halo, we detected a fraction of Sqh-positive puncta along the presynaptic actin core (**Fig. 2F**, **Fig. S3A**, **Supp. Movie S5**). This result suggests that the linear actin structure and NMII together might form a presynaptic actomyosin core with contractile properties.

Non-muscle myosin II regulates the integrity of the presynaptic actin core

The contractility and structural integrity of ventral stress fibers is defined by the recruitment of NMII and the presence of tension[9]. To assess how NMII might regulate the presynaptic actin cytoskeleton, we imaged QmNGMA-labeled F-actin in control and *Zip*^{65947}-expressing larvae and observed reorganization of both round and linear presynaptic actin assemblies (**Fig. 3A-B**; **Supp. Movies S6-7**). We implemented the WEKA classifier to segment and analyze these assemblies as separate categories (see **Fig. S1A-C** for details). While the overall F-actin levels were comparable in both genotypes (**Fig. 3C**), we detected a decrease in the number of actin spots (**Fig. 3D**) and in the percentage of NMJ area covered with linear F-actin (**Fig. 3E**). The remaining round F-actin structures in *Zip*^{65947} mutants were comparable in size and brightness to controls (**Fig. 3D**). On the other hand, the linear actin assemblies were smaller and dimmer in mutant NMJs as compared to controls (**Fig. 3E**, **Supp. Movies S6-7**). We observed and quantified a comparable disorganization of presynaptic actin assemblies in fixed *Zip*^{65947} larvae (**Fig. S5A-B**). These findings demonstrate that NMII is an important regulator of presynaptic actin organization, and of the linear actin core in particular.

Presynaptic NMII- and actin rearrangements can be sensed and propagated transsynaptically

In addition to the presynaptic localization of NMII^{LC}/Sqh::GFP at NMJs of control larvae, we detected a distinct population of dynamic Sqh in the postsynaptic muscle proximal to boutons (**Fig. 2F** and **Supp. Movie S5**). This area contains the subsynaptic reticulum, a postsynaptic membrane specialization enriched with ion channels, cell adhesion molecules, and receptors that facilitate the neuron-to-muscle contact[49]. Postsynaptic Sqh signal was also visible in fixed controls (**Fig. 4A**). Neuron-specific expression of *Zip*^{65947} and *Zip*^{36727} RNAi lines decreased presynaptic Sqh (**Fig. 4A-B**), similar to the decrease in axons (**Fig. S4B-D**). Interestingly, we also observed a decrease in postsynaptic Sqh::GFP signal, both in the region proximal to the bouton as well as in general in the muscle, albeit to a lesser extent (**Fig. 4A** and **C**, **Fig. S4E-F**). To rule out the possibility that this postsynaptic decrease upon neuronal RNAi expression is due to a leaky expression of the transgenic *UAS-RNAi* lines in the muscle, we measured postsynaptic Sqh::GFP levels in larvae carrying control and *Zip RNAi* lines in the absence of the neuronal driver *C155-Gal4*. We confirmed that the decrease in postsynaptic Sqh::GFP levels depends on neuronal, *C155-Gal4*-driven expression of the *NMII/Zip RNAi* lines (**Fig. S4G-H**). WEKA-based analysis of segmented pre- and postsynaptic Sqh-positive particles confirmed a significant decrease in the number, size, and brightness of the NMII structures in *Zip* mutants compared to controls (**Fig. 4B-C**). These data demonstrate that neuronal NMII depletion results in transsynaptic decrease of the motor in the muscle. Thus, impaired neuronal actomyosin assemblies might change the tension in neurons and the presynaptic compartment and propagate these effects transsynaptically to the muscle.

Presynaptic actomyosin depletion alters the organization of Integrin-β receptors

The linear presynaptic actin core shares several features with other mechanosensing and mechanotransducing assemblies, including its molecular composition, its dependence on the presence of the contraction- and tension-inducing NMII motor, as well as the ability to propagate cytoskeletal changes transcellularly. Next, we set out to determine if the presynaptic actomyosin core cooperates with the transmembrane Integrin receptors to facilitate the transsynaptic propagation of actomyosin changes at the NMJ, by exploring the distribution of the *Drosophila* Integrin-β PS subunit Myospheroid/Mys. We used a ubiquitously expressed Integrin-β PS subunit, tagged with YFP (ubiMys::YFP)[50] to visualize Mys in live, dissected larvae (**Fig. 5A**), and a well-characterized antibody[30, 31] to visualize Integrin-β in fixed larvae (**Fig. 5B**). In live larvae, we observed a fraction of ubiMys::YFP Integrin-β formations aligned along the Lifeact::Halo-labeled linear actin core (**Fig. 5A**, **Fig. S6A**, **Supp. Movie S8**). Similar linear Integrin-β formations were detectable in fixed larvae (**Fig. 5B**), and in a previous report[30]. In both conditions, we also detected spot-like

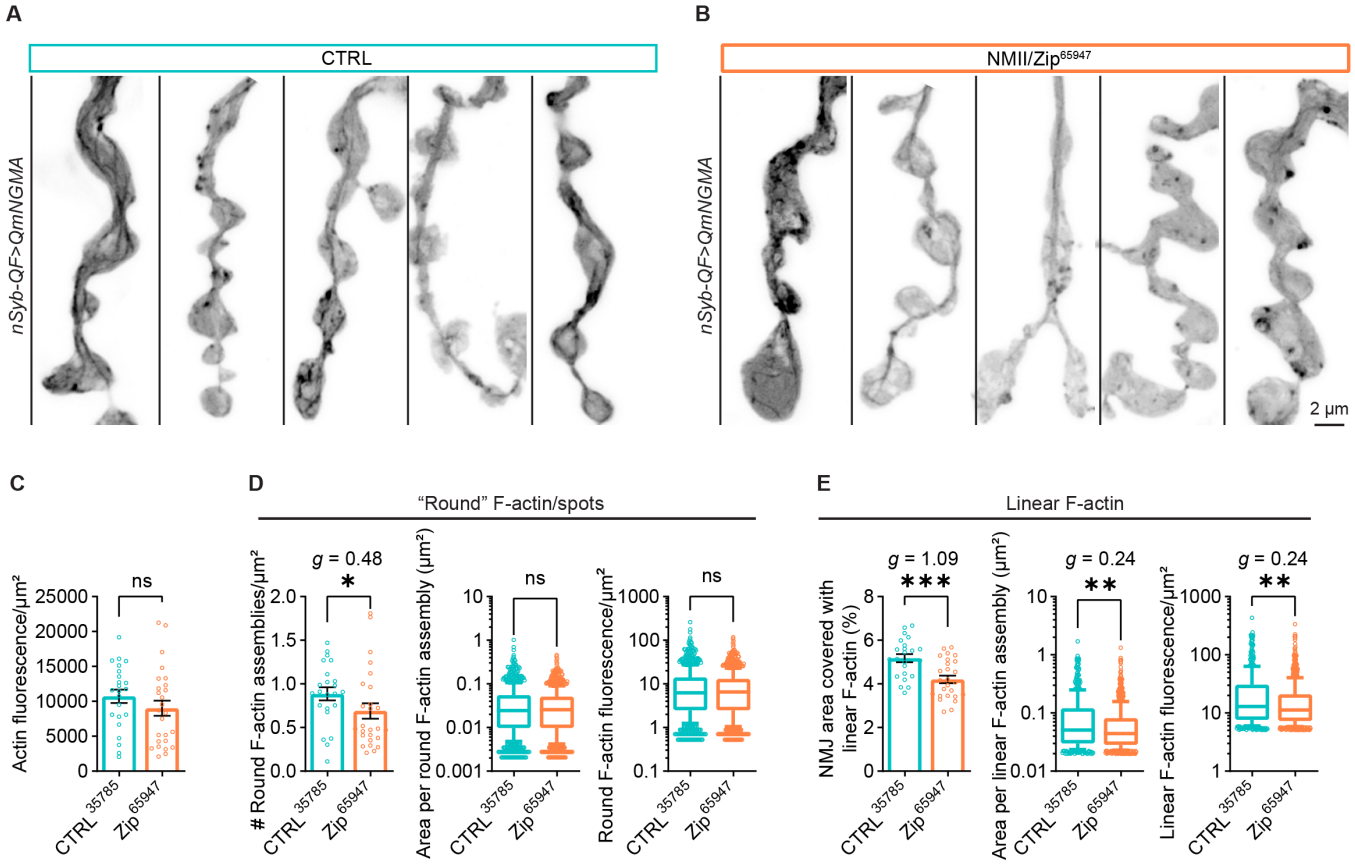

Fig. 3. Non-muscle Myosin II regulates the integrity of presynaptic actin assemblies by. A) QmNGMA-labeled presynaptic actin in larvae co-expressing *CTRL*- or **B**) *NMII/Zip*^{65947} RNAi (see also **Supp. Movies S6-7**.). Representative NMJs are from independent larvae. **C**) Quantification of fluorescence per µm^2 for the QmNGMA actin marker in whole NMJs. **D**) Quantifications of the number of round F-actin assemblies per µm^2, as well as the area and fluorescence of the individual round presynaptic actin structures. **E**) Graphs representing the percentage of NMJ area covered with linear F-actin, as well as the area and fluorescence of the individual assemblies. Box and whiskers graphs were used to represent the results of the area and fluorescence intensity of the individual presynaptic actin structures. Whiskers represent 10th to 90th percentile, while the rest of the data points are shown as individual values. The Y-axis in these graphs represents log10, to capture the broad distribution of the individual values. In bar graphs with linear Y-axis, error bars represent SEM. N in bar graphs – NMJs; N in box and whiskers – individual actin assemblies. ns – not significant, * p<0.05, ** p<0.01, and *** p<0.001 upon unpaired, non-parametric Mann-Whitney test. *g* – Hedges' *g* represents effect size. Scale bars – 2 µm. **See Tables 1 for detailed genotypes and N.**

Integrin-β entities of different sizes both pre- and postsynaptically (**Fig. 5B**), possibly reflecting different stages of maturation of Integrin structures[9, 28, 51], and suggesting a complex fine-tuning of cellular forces at the NMJ.

Next, we examined the effects of NMII on Integrin-β, using the *Zip*^{65947} RNAi tool (**Fig. 5C**). Both visually, upon analysis in the presynaptic compartment, as well as using WEKA-segmented particle analysis, we observed a significant decrease of the presynaptic Integrin-β at *Zip*^{65947} NMJs, accompanied with reduction in the abundance of linear formations at the synapse, as well as in size and intensity (**Fig. 5C-E**). Next, we evaluated presynaptic Integrin-β spots and found that *Zip*^{65947} NMJs had fewer, smaller, and dimmer entities (**Fig. 5F**). Interestingly, we also observed a significant decrease of postsynaptic Integrin-β in the bouton proximity at *Zip*^{65947} NMJs, along with reduced number, size, and intensity of the postsynaptic spots (**Fig. 5G**). We verified that the Integrin-β changes are due to the depletion of NMII by using the independent *Zip*^{36727} RNAi line, which also reduced pre- and postsynaptic Integrin-β levels at NMJs (**Fig. S6B-C**). Next, we confirmed that in absence of the Gal4 driver, the *Zip RNAi* line does not significantly decrease Integrin-β levels at the NMJ (**Fig. S6D-E**). In addition, Integrin-enriched myotendinous junctions[50] in larvae neuronally expressing *CTRL*- and *Zip*^{65947} (*C155-Gal4>RNAi*) had comparable levels of Integrin-β (**Fig. S6F-G**), suggesting that the transsynaptic effect of the presynaptic actomyosin rearrangements on Integrins is local, in proximity to the NMJ. In sum, these data suggests that the linear presynaptic actomyosin core is coupled to transmembrane Integrin receptors to sense and transduce changes in tension at the neuron-muscle interface.

Mechanical severing of neurons rearranges the presynaptic linear actin

In the data presented thus far, we used chronic RNAi-mediated decrease of the levels of the NMII motor to test the integrity and mechanosensitivity of the presynaptic actin core. To assess how acute loss of neuronal tension affects the core, we mechanical disrupted motor neuron tension via axotomy close to the ventral ganglion (**Fig. 6A**), similar to studies of the effects of mechanical tension on synaptic vesicle distribution[20], albeit at different developmental stage. This procedure is widely used in the field, as it prevents excessive muscle contraction in larval fillets, while the preparation maintains muscle potential and capacity for evoked neurotransmitter release[52]. We analyzed presynaptic

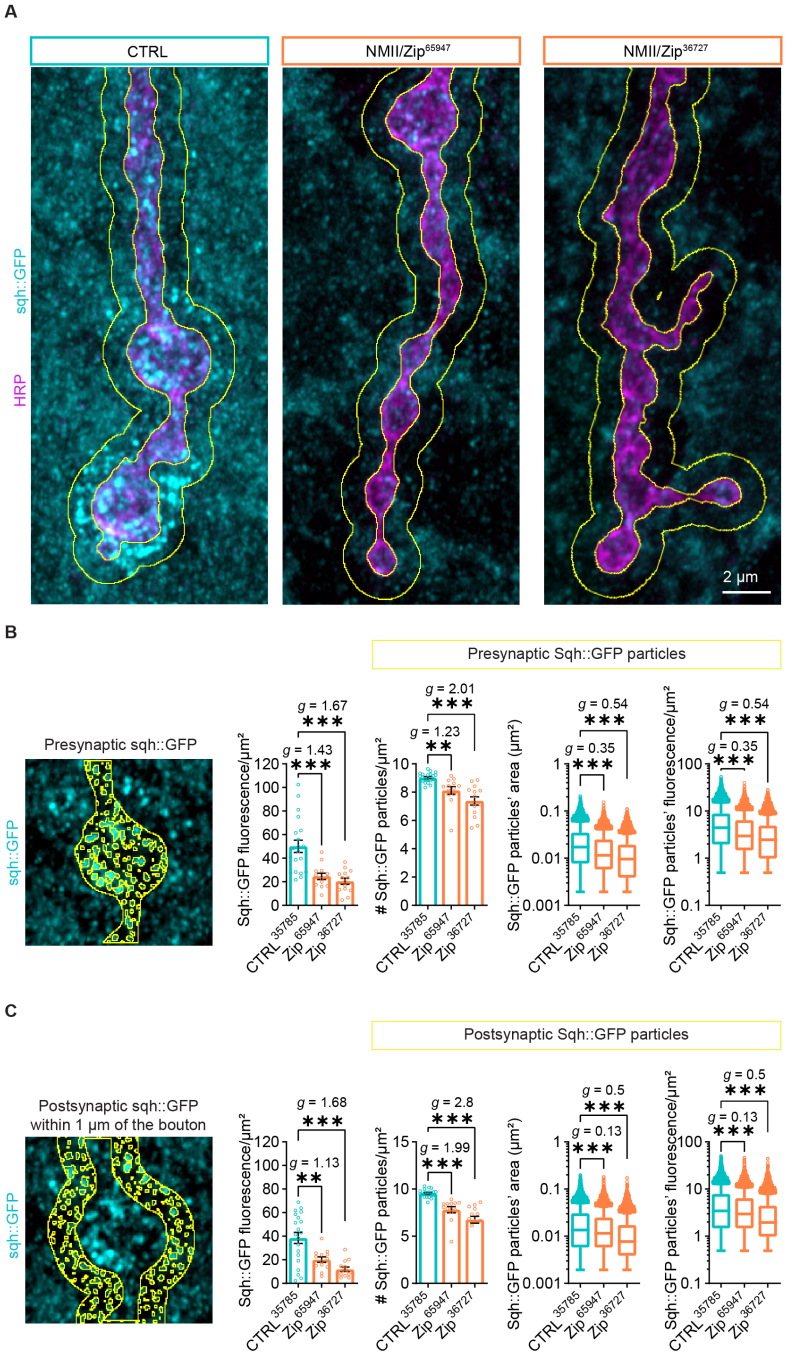

Fig. 4. Depletion of neuronal NMII reduces the levels of the motor in the muscle. A) Sqh::GFP-labeled NMII at NMJs in fixed larvae expressing *CTRL*^{35785}, *Zip*^{65947}, and *Zip*^{36727} RNAi in neurons (*C155-Gal4*). Sqh::GFP particles were analyzed in the presynaptic area (masked by the neuronal a-HRP signal, inner yellow outline) as well as 1 µm outside the neuron in the postsynaptic area (outer yellow outline). **B**) Analysis of the fluorescence per µm^2 of presynaptic Sqh::GFP as well as the number, area and fluorescence of WEKA-segmented individual sqh::GFP particles. **C**) Analysis of the fluorescence per µm^2 of postsynaptic Sqh::GFP as well as the number, area and fluorescence of WEKA-segmented individual sqh::GFP particles. Box and whiskers graphs were used to represent the results of the area and fluorescence intensity of the individual Sqh particles. Whiskers represent 10th to 90th percentile, while the rest of the data point are shown as individual values. The Y-axis in these graphs represents log10, to capture the broad distribution of the individual values. In bar graphs with linear Y-axis, error bars represent SEM. N in bar graphs – NMJs; N in box and whiskers – individual actin assemblies. ** p<0.01, *** p<0.001 after one-way ANOVA with Šídák's multiple comparisons test. *g* – Hedges' *g* represents effect size. Scale bar – 2 µm. **See Table 1 for detailed genotypes and N.**

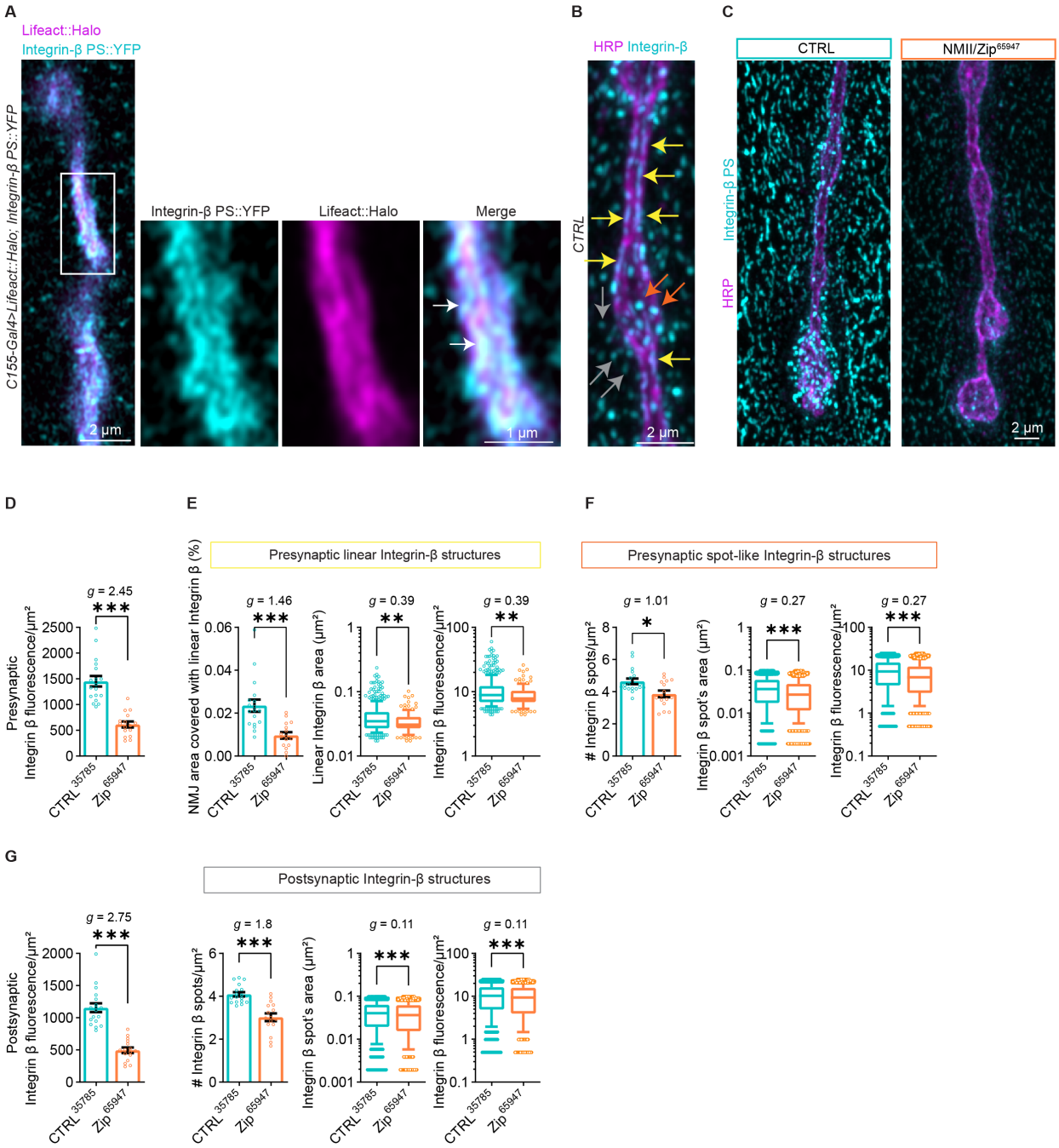

Fig. 5. Neuronal depletion of non-muscle Myosin II rearranges Integrin receptors at the NMJ. A) Distribution of YFP-tagged, ubiquitously expressed Integrin-β (cyan) at NMJs in live larvae expressing Lifeact::Halo (magenta) in neurons (see also **Supp. Movie S8**). White arrows point to areas of overlap between Integrin-β and linear F-actin. **B**) Immunostaining of Integrin-β (cyan) at NMJs of control larvae. Yellow arrows depict Integrin-β in linear structures, red arrows point to presynaptic spot-like Integrin-β structures, while gray arrows point to postsynaptic spot-like Integrin-β. **C**) Reorganization of Integrin-β at NMJs of larvae expressing *Zip*^{65947} in neurons, compared to controls. **D**) Analysis of the fluorescence per µm^2 of presynaptic Integrin-β. **E**) Quantification of the percentage of NMJ area occupied by linear Integrin-β structures, as well as the area and fluorescence of WEKA-segmented individual particles. **F**) Analysis of the number of presynaptic Integrin-β foci and the area and fluorescence of WEKA-segmented individual particles. **G**) Analysis of the fluorescence per µm^2 of postsynaptic Integrin-β, as well as the number of postsynaptic Integrin-β foci and the area and fluorescence of WEKA-segmented individual particles. Box and whiskers graphs were used to represent the results of the area and fluorescence intensity of the individual Sqh particles. Whiskers represent 10th to 90th percentile, while the rest of the data points are shown as individual values. The Y-axis in these graphs represents log10, to capture the broad distribution of the individual values. In bar graphs with linear Y-axis, error bars represent SEM. N in bar graphs – NMJs; N in box and whiskers – individual Integrin-β assemblies. Ns – non-significant, * p<0.05, ** p<0.01, and *** p<0.001 upon unpaired, non-parametric Mann-Whitney test. *g* – Hedges' *g* represents effect size. Scale bars – 2 µm, inset in **A**) with scale bar – 1 µm. **See Table 1 for detailed genotypes and N.**

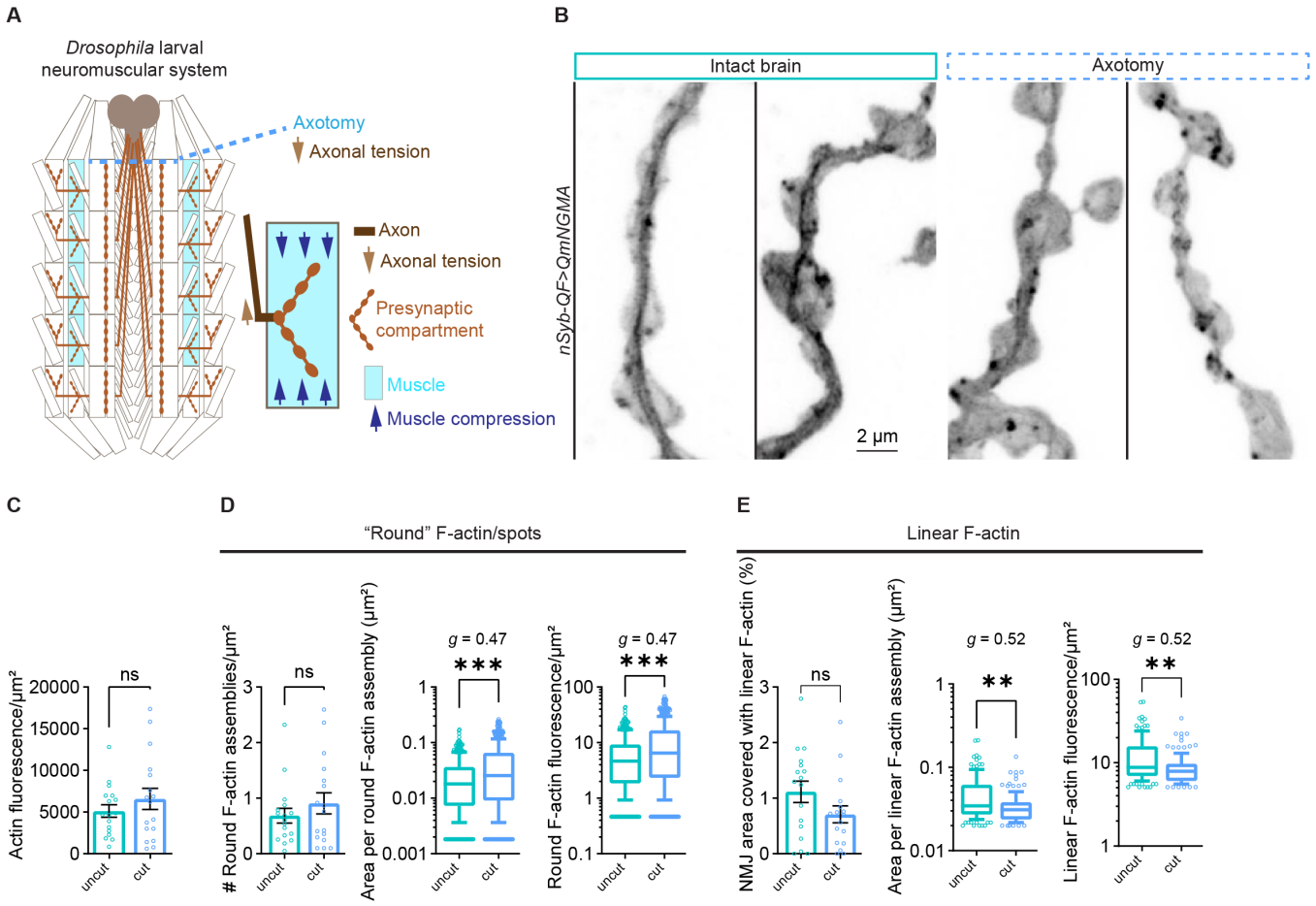

Fig. 6. Mechanical severing of larval axons induces changes in presynaptic F-actin. A) Diagram of *Drosophila* fillet preparation upon axotomy (light blue dashed line) of all proximal neurons descending from the larval brain. This procedure removes the axonal tension exerted at presynaptic compartments. **B**) mNGMA-labeled presynaptic actin at NMJs from live larvae with intact brains (left) or upon severing of the brain/axotomy (right) (see also **Supp. Movies S9-10**). **C**) Quantification of the fluorescence per µm^2 for the QmNGMA actin marker in whole NMJs. **D**) Quantifications of the number of round F-actin assemblies per µm^2, as well as the area and fluorescence of the individual round presynaptic actin structures. **E**) Graphs representing the percentage of NMJ area covered with linear F-actin, as well as the area and fluorescence of the individual assemblies. Box and whiskers graphs were used to represent the results of the area and fluorescence intensity of the individual presynaptic actin structures. Whiskers represent 10th to 90th percentile, while the rest of the data points are shown as individual values. The Y-axis in these graphs represents log10, to capture the broad distribution of the individual values. In bar graphs with linear Y-axis, error bars represent SEM. N in bar graphs – NMJs; N in box and whiskers – individual actin assemblies. ns – not significant, ** p<0.01, and *** p<0.001 upon unpaired, non-parametric Mann-Whitney test. Error bars represent SEM. *g* – Hedges' *g* represents effect size. Scale bar – 2 µm. **See Table 1 for detailed genotypes and N.**

actin assemblies labeled with neuronal QmNGMA, in larvae with intact versus cut axons; larvae were imaged live within ~20 minutes after axotomy (**Fig. 6A**, **Supp. Movies S9-10**). Larvae with severed axons had similar total levels of F-actin at the NMJ compared to controls with intact axons, with no significant changes in the number of spot-like and linear actin assemblies (**Fig. 6B**). However, WEKA classifier-based segmentation of presynaptic actin subpopulations in the two conditions revealed an increase in the area and brightness of round actin structures (**Fig. 6C**) and a decrease of the same parameters for the linear F-actin assemblies upon axotomy (**Fig. 6D**). Thus, mechanical discontinuation of neuronal integrity via severing of distal axons is sensed at the presynaptic terminal, where the presynaptic actin core was disrupted, in a manner similar to neuronal NMII depletion.

Discussion

Multicellularity requires intracellular molecular machineries that sense and integrate the dynamics of the extracellular environment and of neighboring cells and tissues. This balance becomes especially important when the structural, biochemical, and mechanical properties of interacting cells and tissues are different, posing a challenge to the long-term maintenance of their contact. The neuromuscular junction is an impressive metazoan solution to these mechanical challenges, yet our knowledge on the molecular mechanisms involved remains limited. Here we show that a novel presynaptic actin structure responds to mechanical forces and is implicated in transynaptic effects on adhesive and contractile machinery.

The vast majority of mechanobiology studies of neurons come from cells in culture, from which we have learned that every stage of neuronal development, differentiation and maturation depends on the neuronal cytoskeleton, including contractile actomyosin and Integrin receptors[53]. How mechanical forces are sensed, generated, and transmitted within neurons and their surrounding muscles in the context of the animal remains understudied for several reasons. Neuronal compartments are relatively small, and actomyosin components are organized into submicron structures visible only with superresolution microscopy[11, 16]. Even with recent advances in imaging technologies, the actin

cytoskeleton is inherently sensitive to fixation, and using genetically-encoded actin markers to visualize the cytoskeleton live has its own challenges and caveats[54]. Differentiating between the actomyosin content of two closely apposed cells poses additional constraints. In this study, we addressed these challenges by using the *Drosophila* larval NMJ as a tissue mechanics model, that can be accessible via a broad range of genetic interventions and live imaging. We used multiple complementary genetically encoded actin markers, combined with genetic tools that facilitate tissue-specific visualization. We implemented Airyscan microscopy for improved resolution and a signal-to-noise, and finally, we used machine-learning-based segmentation to facilitate unbiased analyses of distinct actin assemblies.

A novel presynaptic actin core may be analogous to ventral stress fibers

Using these tools, we identified subpopulations of presynaptic actin assemblies as possible candidates for mechanosensitive structures. We further characterized linear actin assemblies which predominantly traverse through the center of the NMJ, forming a presynaptic linear actin core. Our live imaging and FRAP experiments demonstrated that the actin core is constituted of long-lived, low turnover linear actin, sensitive to the actin depolymerizing drug LatA. The linear shape of the actin core, as well as its lifetime and turnover dynamics resembled the microns-long ventral stress fibers (VSFs) in adherent cells[9]. We detected the actin stabilizer Tropomyosin on the actin core, representing a molecular signature that facilitates recruitment of NMII and determines the contractile properties in the case of VSFs[44]. Similarly, puncta of the non-muscle myosin II light chain subunit Sqh also decorated the core. At this point, we do not know if the linear actin of the presynaptic core consists of antiparallel actin filaments, a requirement for NMII-based contractility. Based on the depletion of these structures upon neuronal NMII decrease, we assume that they do have antiparallel organization but cannot rule out whether some might have uniform polarity, more similar to yeast actin cables[55].

Interestingly, the VSFs are not polymerized *de novo* but rather generated through a merging of pre-existing stress fiber precursors[56]. Thus, drawing further on the presynaptic actin core-VSF analogy, the lack of specific enrichment of the Arp2/3 or formin/Dia actin nucleators along the core is not surprising. Arp2/3 nucleation is crucial for rapid force-generating events like endocytosis[4, 5], as well as the formation of mesh-like structures proximal to active zones in bead-induced synapses[18]. Similarly, formins are important for assembly of presynaptic actin[18]. From our FRAP data we can deduce that these structures might not be rapidly nucleated *de novo*, but similarly to the VSFs depend on the local availability of pre-assembled actin filaments.

One of the strongest functional analogies between the presynaptic actin core and ventral stress fibers is their force-dependent assembly[56]. We took advantage of the *Drosophila* model and targeted NMII directly by neuronal depletion of both the heavy chain and light chain of NMII. Interestingly, we observed major perturbations of presynaptic actin subpopulations, including of the linear presynaptic actin core. These results further indicated that the linear actin core is a good candidate to be an actomyosin contractile structure. Interestingly, we also observed a transsynaptic change in NMII levels in the muscle upon neuronal Zip down-regulation. This finding raised the possibility that the actomyosin core, similarly to the VSFs, is coupled to focal adhesions and Integrin receptors, and can regulate Integrins via inside-out activation, perhaps via mechanosensitive cytoskeletal linker proteins such as spot-like Talin and vinculin[57]. The inside-out activation of Integrins could trigger two crucial events: 1) binding of additional cytoplasmic effectors that mediate the activation but also clustering of Integrins into a range of early nascent adhesions to mature focal adhesions[58]; and 2) conformational changes on the Integrin extracellular domains, facilitating interactions with the ligands of the ECM[59] or on the neighboring tissue, i.e., the muscle. Thus, in the absence of functional presynaptic actomyosin this route of inside-out Integrin activation could be defective, resulting in a decrease of presynaptic but also postsynaptic Integrin foci, while the ones that still form do not reach wild-type size (and possibly composition). These Integrin changes at the neuron-muscle interface would then have a transsynaptic effect on the levels of the NMII motor in proximity to the NMJ, but not on Integrin accumulations further away at the myotendinous junctions. On the other hand, muscle contractions exert mechanical force on neurons and Integrins are also mechanically activated via this outside-in mechanosensing[60]. However, the decreased levels of Integrins induced by the defective presynaptic actomyosin inside-out signaling probably also decrease the mechanoresponsiveness to muscle contractions thus preventing this feedback mechanism and impairing synaptic plasticity in a range of activity-dependent paradigms at the *Drosophila* NMJ[29, 31, 32].

Interestingly, we identified linear and round Integrin-β entities, suggesting that they might have distinct assembly mechanisms and putative ligands. This is not a surprise, knowing that in mammals, pairing 8 β-subunits to 18 α-subunits can generate 24 functionally distinct Integrin heterodimers, while in *Drosophila* the β-subunit we studied can pair to five α-subunits[61]. In addition, the different heterodimers can have limited or multiple ECM ligands, or the same ECM ligand can interact with different Integrins[62]. At the NMJ, excessive Tenectin disrupted the postsynaptic Integrin-β subpopulation, which facilitated the visualization of the linear entities, suggesting that only a fraction of the Integrin receptors is sensitive to the neuronal overexpression of this secreted ECM molecule[30]. Integrins can be arranged and aligned by the actin cytoskeleton[63], and we observe partial alignment between the linear Integrin-β subpopulation and the presynaptic actin core. Moreover, the decrease in both linear and round Integrin-β entities upon neuronal NMII depletion points to the presynaptic actomyosin core as an important regulator of the assembly of Integrins at the NMJ. In addition, we detected Integrin-β entities with different sizes even in wild type conditions, possibly reflecting different stages of maturation[51]. Indeed, expansion and activation of Integrin and Talin-based foci were recently correlated with homeostatic synaptic plasticity at the *Drosophila* NMJ[28]. From these findings we hypothesize that synapses use a multi-tier system of Integrin-based adhesions to accommodate synaptic function and plasticity. In addition, we suggest a model in which neurons behave as a mechanical continuum that induces and transmits changes in tension in concert with the transmembrane Integrin receptors.

The role of actomyosin in supporting a mechanical continuum in neurons

The presynaptic compartment at the NMJ is the most distal part of the motor neuron, experiencing not only the contractile forces of the muscle but also the pulling forces of axons. Advances in super-resolution microscopy have identified characteristic axonal organization of actin rings interconnected by spectrin repeats. The periodic organization of these cytoskeletal elements recruits numerous supporting molecules (required for action potential propagation, cell adhesion etc.), and is functionally important for axon-axon and axon-dendrite interactions[14]. Additionally, this submembraneous cytoskeleton acts as a mechanical scaffold and tension buffer system for strained axons[64]. Interestingly, NMII was identified as part of the SMC. Imaging and functional analysis of the role of NMII suggested that SMC-associated NMII regulates axonal diameter and conduction[12, 14], as well as bulky cargo transport[15], supporting a predominant view in the field that the SMC actomyosin regulates radial contractility. Pharmacological inhibition of NMII or knockdown of both NMIIA and B in hippocampal neurons changes the axon diameter while the periodicity of the SMC remains unchanged[12, 14]. These results contrast with our findings where we observe major actin rearrangements at the NMJ, suggesting that compared to axonal NMII,

presynaptic NMII is a major regulator of actin integrity, most importantly of the mechanosensitive linear actin core.

In addition to the SMC, longitudinal, linear actin bundles distinct from the subplasmalemmal actin rings were identified "deeper" in axon shafts of live hippocampal neurons[17, 65], DRG sensory cultured neurons[66], as well as sensory neurons in *C. elegans*[67]. These actin trails are dynamic, bidirectional structures, and unlike the linear actin core that we observed traversing throughout NMJs, they frequently terminated at boutons and were therefore considered to be an actin delivery system for *en-passant* synapses[17]. At this point, it seems that the actin trails and the presynaptic actin core are distinct, though we cannot exclude that they might have overlapping functions, including the maintenance of local actin pools. If generated via mechanisms similar to VSFs, i.e., by repurposing actin filaments into actomyosin structures, then the presynaptic core could serve a dual role as both a mechanosensitive structure and a reservoir for actin at the distal presynaptic compartment. Axonal actin trails were strongly dependent on functional formins, though this was tested with a moderate SMIFH2 concentration (30 µM) which is known to have off-target effects on NMII motor activity[68]. Thus, it would be interesting to see if the axonal actin trails diminish upon NMII knockdown similarly to what we observe for the presynaptic linear actin core.

Our experiments demonstrate that axotomy of the neurons projecting to the NMJ induces similar fragmentation of the presynaptic actin core to NMII neuronal depletion. This suggests that there is either a continuous component or a relay that facilitates this sensitivity. We envisage a spring-like tension sensor that traverses the whole neuron, from the cell body up to the terminals. On the other hand, compartmentalized mechanical strain-mitigating strategies might be employed via local cytoskeletal remodeling[69]. Our data indicate that a component of this tension sensor at the axon terminal is actomyosin-based. Whether this presynaptic actin core is part of a larger physical mechanical continuum remains to be clarified by more detailed studies of the rest of the axonal continuum in the future.

In cultured neurons, growth cones are the most distal tip of growing axons. They are also dynamic, F-actin-rich structures heavily depended on regulated actin polymerization/depolymerization cycles[70]. Interestingly, growth cones collapse, along with decrease in the F-actin levels and SMC disorganization, are early events in both axotomy and nerve growth factor withdrawal (NGFW)-induced axonal degeneration paradigms[66, 71] Moreover, the abundance of actin trails also declined at the early stages of NGFW, further supporting the idea that remodeling of actin assemblies is a major component of axonal degeneration[66]. These findings are reminiscent of our observations of a defective presynaptic actin core upon NMII neuronal depletion or axotomy. Thus, the presynaptic actin assembly we identified at the NMJ could be a potential target for neurodegeneration-associated cytoskeletal rearrangements. Of note, we recently described an actin cytoskeleton-based component as a pathomechanism in a subtype of peripheral neuropathy (Charcot-Marie-Tooth/CMT), induced by the actin-binding function of tyrosyl- and other aminoacyl-tRNA synthetases[72]. We observed rearrangements of the actin cytoskeleton at NMJs of the CMT *Drosophila* model, as well as disorganization of stress fibers in CMT patient-derived fibroblasts. Therefore, the presynaptic linear actin core that we described in the current study not only regulates the mechanobiology of the NMJ in health but also represents an excellent candidate structure to be studied in *Drosophila* models of neuromuscular disorders.

Methods

Drosophila maintenance and genetics

Drosophila melanogaster stocks were raised on a standard cornmeal medium. Crosses were maintained at 25° C, on 12 h light-dark cycles. Detailed genotype information (including sex) of larvae is listed in the source data table and **Table 1**.

Drosophila clones and generation of transgenic flies

The following clones were generated by nucleotide synthesis at VectorBuilder, Inc (Chicago, IL): mNeonGreen::GMA (GMA sequence described in[1]), mNeonGreen::Tm1 isoform A (NCBI Accession: NP_524360.2), mNeonGreen::Tm1 isoform L (Accession: NP_996216.1), and mScarlet-I::Act5C (NCBI Accession: NP_001284915.1). These constructs were then subcloned into pQUAST-attB (DGRC Stock 1438 ; https://dgrc.bio.indiana.edu//stock/1438; RRID:DGRC_1438). All plasmids were sequence verified (IDG and Plasmidsaurus, Inc). Transgenic flies carrying these constructs were generated at BestGene, Inc., using the PhiC31 system at attP40 or attP2 landing sites (see source data table).

Dissection procedures for live imaging experiments

Third instar larvae with the desired genotype were held by two pins (anterior and posterior), dissected in Ca^{2+}-free HL3.1 (pH 7.2)[2] and immediately transferred to a microscopic slide in ~50 µl. HL3.1 The larva was then sandwiched using permanent double-sided tape spacers (Scotch 3M ID CBGNHW011141) and a No. 1.5 glass coverslip, and imaged immediately. When two different conditions were tested (e.g. LatA treatment and DMSO, or intact brain and axotomy), we mounted pairs of larvae, and alternated the order in which the two conditions were imaged between pairs. For the Latrunculin A treatment, 1 mM InSolution Latrunculin A (Sigma-Aldrich, 428026) in DMSO was brought to a concentration of 1 µM with HL3.1 dissection medium. As a vehicle control, we used 100% DMSO, similarly dissolved 1000x in HL3.1. Two larvae were dissected as described above, with one undergoing a 30-minute incubation in LatA while the other was incubated in DMSO (in separate Sylgard-coated small Petri dishes). After the incubation, the larvae were washed with 500 µl HL3.1 once, and immediately mounted on a microscopic slide for imaging, as described above. To visualize the Lifeact::Halo actin marker, dissected larvae were incubated in HL3.1 with 2 µM Janelia Fluor® HaloTag® Ligand-549 for 5 minutes, and directly mounted in ~50 µl HL3.1 without additional washing. For the axotomy experiment, two larvae were dissected in parallel, then just before mounting, we cut the axons (close to the ventral ganglion) from one larva. Larvae were imaged within 20 minutes of axotomy, on average.

Drosophila immunohistochemistry

Larvae were dissected in HL3.1 (pH 7.2) in a Sylgard-coated dissection dish, fixed for 10 minutes in 4% PFA in HL3.1, washed 3 x 15 minutes in 1xPBS, and permeabilized with 0.1 % PBX (1xPBS with Triton-X) for 3 x 5 minutes. Incubation with the primary antibody was performed either for 2 hours at room temperature, or overnight at 4° C. After a wash (3 x 5 minutes in 0.1 % PBX), the samples were incubated with secondary antibody for 1 hour, followed by a final wash in 0.1 % PBX. Larvae were mounted in ProLong™ Diamond Antifade Mountant (Invitrogen) and cured at room temperature for 48-72 hours before imaging. HRP-Red Rhodamine was used at 1:250. The GFP signal of Sqh::GFP was enhanced by staining with FluoTag®-X4 anti-GFP (NanoTag Biotechnologies, 1:250). Mouse monoclonal anti-Integrin beta PS (DSHB CF.6G11, 1:50) primary, and Alexa Fluor® 488 AffiniPure Goat Anti-Mouse IgG (H+L) secondary (Jackson ImmunoResearch) antibodies were used to detect Integrin at the NMJ. Rabbit anti-Tm1 (D. Montell, 1:500, precleared by incubation with dissected, fixed and permeabilized w^{1118} larvae) and Alexa Fluor® 488 AffiniPure Goat Anti-Rabbit IgG (H+L) (Jackson ImmunoResearch) secondary antibodies were used to detect Tm1-A/L at the NMJ. Rhodamine Red™-X (RRX)

AffiniPure Goat Anti-Horseradish Peroxidase (Jackson ImmunoResearch) was used to detect the neuronal membrane of NMJs and axons.

Microscopy

All imaging was performed on an inverted Zeiss LSM 880 microscope with an Airyscan 2 detector, using the 63X oil immersion objective (NA 1.4). Raw images were subjected to 3D Airyscan processing with default settings in Zen Black software. Z-stacks of NMJs in fixed larvae were captured at voxel size (0.044 x 0.044 x 0.185) µm. Z-stacks of NMJs in live larvae were captured with a pixel size 0.044 x 0.044 µm, and Z-step varying from 250-500 µm. For the FRAP experiment, we used NMJs with clearly visible actin core, photobleached them at 100% laser power, and followed the recovery of the signal for 90 seconds with 1 Hz sampling frequency.

Image analysis

All image analyses were performed in FIJI[3]. Unless otherwise stated, we used maximum intensity projections for all image analyses.

For measuring the fluorescence intensity per μm^2 of the signals-of-interest in the presynaptic compartment of fixed samples, we segmented and masked NMJs using the HRP signal. The HRP signal was also used to clean parts of images containing axons and debris when analyzing the presynaptic compartment of the NMJ. Before analyzing images with Sqh::GFP we cropped out sections HRP-labeled NMJ in proximity to glia, trachea or axons (all compartments where Sqh::GFP under its own promoter is enriched in a distinct pattern from the spot-like signal at the NMJ). This way we prevented measuring of irrelevant non-neuronal or non-muscle Sqh::GFP signal. To obtain a mask the following steps were run on maximum intensity projections: Gaussian Blur with sigma=2 > Auto Threshold method – Huang > Convert to Mask > Erode.

When measuring fluorescence per μm^2 of dim signals present in both the pre- and post-synaptic compartments of the NMJ (like Sqh::GFP), the background fluorescence per μm^2 (measured in areas where no signal enrichment was observed) was subtracted from the neuronal fluorescence per μm^2.

For the remaining image analyses, NMJs were masked using the fluorescently tagged actin or actin marker, or Tm1 (using the HRP masking work flow). To specifically analyze objects in the 1 µm ring surrounding the boutons, we used the "enlarge" function to extend the neuronal mask by 1 µm, and used the XOR function in FIJI to intersect that specific region.

In the data presented in **Fig. S2F-G** (LatA treatment of larvae expressing the actin marker QmNGMA in neurons), we generated a WEKA classifier[4] that masks the NMJ core, and determined changes in F-actin fluorescence in this area of interest.

Segmentation and analysis of individual F-actin assemblies: We built a two-class WEKA classifier by manually annotating round and linear F-actin (**Fig. S1A-C**). The classifier was applied to the first frame of the captured movies and separate probability maps of round and linear F-actin assemblies were obtained as a 32-bit images. In the next step of the image analysis pipeline, we used batch processing to perform particle analysis in Fiji. Round and linear F-actin particles were masked and analyzed separately.

The 32-bit probability map image of linear F-actin after applying the WEKA classifier gave good coverage of predominantly linear structures (**Fig. S1B**). Next, the 32-bit image was transformed to a 16-bit one, which was further used to generate a binary mask. The probability map to binary image transition included more F-actin structures than the linear population. By optimizing the subsequent steps, we designed a pipeline where the binary mask of linear F-actin was further despeckled and skeletonized. Further particle analysis of the skeletonized mask performed with a size cutoff=0.02 μm^2-Infinity and a circularity cutoff=0.00-0.20, ensuring that the majority of analyzed particles represented linear F-actin structures. The 32-bit probability map image of round F-actin after applying the WEKA classifier similarly gave good coverage of spot-like structures (**Fig. S1C**), while the transition to binary mask did not introduce many linear actin structures. To better segment individual round assemblies, the binary mask underwent despeckling and erosion. All round F-actin particles larger than 0.0018 μm^2 were included in the analysis. In general, our image analysis pipeline is powerful in providing unbiased and high throughput analysis of specific, individual F-actin assemblies at the synapse. However, we think that it underestimates the size and brightness of these structures as a result of our efforts to segment and analyze them as individual, largely non-overlapping entities.

Segmentation and analysis of individual Sqh- and Integrin particles: we built single-class WEKA classifiers that were trained by manually annotating the Sqh or Integrin structures. The classifiers were applied to the maximum intensity projections of the Sqh or Integrin channels, accordingly. The obtained masked Sqh::GFP particles were despeckled and eroded before finally analyzed with no size or circularity filters. To distinguish between linear and round Integrin entities, the following cut-offs we applied at the particle analysis step: for spot-like integrin, a size cut-off of 0.1 μm^2, and a circularity cut-off 0.21-1; for linear integrin analysis we first skeletonized the segmented entities and analyzed particles with a size higher than 0.0018 μm^2 and a circularity between 0-0.2. Pearson's correlation coefficient was calculated using the CoLoc Plugin in Fiji.

Statistics

We used GraphPad Prism V9 for statistical analyses and generation of graphs. Data were not tested for normality and nonparametric tests were used for analyses. Mann-Whitney tests were used when analyzing two conditions, and one-way ANOVA with, Kruskal-Wallis or Sidek tests with multiple comparison were used to determine the statistical significance of the data from more than two different conditions. To determine the effect size, we measured Hedges' *g* value, which we also added to graphs. We calculated Hedges' *g* using the following formula: $g = M_1\text{-}M_2/SD_{pooled}$, where $M_1 - M_2$ is the difference in means, while SD^*_{pooled} is the pooled and weighted standard deviation. We used bar graphs or box and whiskers graphs to represent our data. In the bar graphs, the error bars represent standard error of mean (SEM). In the box and whiskers graphs, the whiskers are drawn down to the 10th percentile and up to the 90th percentile. Data points below or above the whiskers are shown as individual points. The line passing through the box represents the median. We used logarithmic scale along the Y axis to display the wide range of values for the area and fluorescence of the different actin assemblies, sqh- and integrin particles in a compact way. The FRAP curves in **Fig. 1F** and **Fig. S2D** were constructed after measuring the fluorescence intensity per μm^2 within the bleached region, as well as in a non-photobleached region to account for the background photobleaching during imaging. The measured values were normalized to the maximum fluorescence intensity value and fitted into a double-exponential curve in GraphPad.

Acknowledgements:

We thank the *Drosophila* Genomics Resource Center (NIH Grant 2P40OD010949); Bloomington *Drosophila* Stock Center (Indiana University, Bloomington, IN, NIH 595 P40OD018537); Guy Tanentzapf for *PUbi-mys.YFP*; and Denise Montell (UCSB) for the Tm1 antibody. This work was supported by NINDS grant R01 NS116375 to A.A.R.

Competing interests: The authors declare no competing interests.

Author contributions: Conceptualization: B.E., A.A.R. Methodology: B.E., A.A.R. Investigation: B.E. Visualization: B.E. Funding acquisition:

A.A.R. Project administration: A.A.R. Supervision: A.A.R. Writing – original draft: B.E. Writing—review & editing: A.A.R.

References:

1. Tyler, W.J. The mechanobiology of brain function. *Nat Rev Neurosci* **13**, 867-878 (2012).
2. Iyer, S.R., Shah, S.B. & Lovering, R.M. The Neuromuscular Junction: Roles in Aging and Neuromuscular Disease. *Int J Mol Sci* **22** (2021).
3. Michelot, A. & Drubin, D.G. Building distinct actin filament networks in a common cytoplasm. *Curr Biol* **21**, R560-569 (2011).
4. Akamatsu, M. *et al.* Principles of self-organization and load adaptation by the actin cytoskeleton during clathrin-mediated endocytosis. *eLife* **9**, e49840 (2020).
5. Del Signore, S.J. *et al.* An autoinhibitory clamp of actin assembly constrains and directs synaptic endocytosis. *eLife* **10**, e69597 (2021).
6. Murrell, M., Oakes, P.W., Lenz, M. & Gardel, M.L. Forcing cells into shape: the mechanics of actomyosin contractility. *Nat Rev Mol Cell Biol* **16**, 486-498 (2015).
7. Vicente-Manzanares, M., Ma, X., Adelstein, R.S. & Horwitz, A.R. Non-muscle myosin II takes centre stage in cell adhesion and migration. *Nat Rev Mol Cell Biol* **10**, 778-790 (2009).
8. Quintanilla, M.A., Hammer, J.A. & Beach, J.R. Non-muscle myosin 2 at a glance. *J Cell Sci* **136** (2023).
9. Livne, A. & Geiger, B. The inner workings of stress fibers - from contractile machinery to focal adhesions and back. *J Cell Sci* **129**, 1293-1304 (2016).
10. Xu, K., Zhong, G. & Zhuang, X. Actin, spectrin, and associated proteins form a periodic cytoskeletal structure in axons. *Science* **339**, 452-456 (2013).
11. Berger, S.L. *et al.* Localized Myosin II Activity Regulates Assembly and Plasticity of the Axon Initial Segment. *Neuron* **97**, 555-570.e556 (2018).
12. Costa, A.R. *et al.* The membrane periodic skeleton is an actomyosin network that regulates axonal diameter and conduction. *Elife* **9** (2020).
13. He, J. *et al.* Prevalent presence of periodic actin-spectrin-based membrane skeleton in a broad range of neuronal cell types and animal species. *Proc Natl Acad Sci U S A* **113**, 6029-6034 (2016).
14. Zhou, R. *et al.* Proteomic and functional analyses of the periodic membrane skeleton in neurons. *Nature Communications* **13**, 3196 (2022).
15. Wang, T. *et al.* Radial contractility of actomyosin rings facilitates axonal trafficking and structural stability. *J Cell Biol* **219** (2020).
16. Vassilopoulos, S., Gibaud, S., Jimenez, A., Caillol, G. & Leterrier, C. Ultrastructure of the axonal periodic scaffold reveals a braid-like organization of actin rings. *Nature Communications* **10**, 5803 (2019).
17. Ganguly, A. *et al.* A dynamic formin-dependent deep F-actin network in axons. *J Cell Biol* **210**, 401-417 (2015).
18. Bingham, D. *et al.* Presynapses contain distinct actin nanostructures. *J Cell Biol* **222** (2023).
19. Seabrooke, S., Qiu, X. & Stewart, B.A. Nonmuscle Myosin II helps regulate synaptic vesicle mobility at the *Drosophila* neuromuscular junction. *BMC Neurosci* **11**, 37 (2010).
20. Siechen, S., Yang, S., Chiba, A. & Saif, T. Mechanical tension contributes to clustering of neurotransmitter vesicles at presynaptic terminals. *Proc Natl Acad Sci U S A* **106**, 12611-12616 (2009).
21. Fernandes, A.R., Martins, J.P., Gomes, E.R., Mendes, C.S. & Teodoro, R.O. *Drosophila* motor neuron boutons remodel through membrane blebbing coupled with muscle contraction. *Nat Commun* **14**, 3352 (2023).
22. Ataman, B. *et al.* Rapid activity-dependent modifications in synaptic structure and function require bidirectional Wnt signaling. *Neuron* **57**, 705-718 (2008).
23. Piccioli, Z.D. & Littleton, J.T. Retrograde BMP signaling modulates rapid activity-dependent synaptic growth via presynaptic LIM kinase regulation of cofilin. *J Neurosci* **34**, 4371-4381 (2014).
24. Vasin, A. *et al.* Two Pathways for the Activity-Dependent Growth and Differentiation of Synaptic Boutons in *Drosophila*. *eNeuro* **6** (2019).
25. Chastney, M.R., Conway, J.R.W. & Ivaska, J. Integrin adhesion complexes. *Curr Biol* **31**, R536-r542 (2021).
26. Park, Y.K. & Goda, Y. Integrins in synapse regulation. *Nat Rev Neurosci* **17**, 745-756 (2016).
27. Beumer, K.J., Rohrbough, J., Prokop, A. & Broadie, K. A role for PS integrins in morphological growth and synaptic function at the postembryonic neuromuscular junction of *Drosophila*. *Development* **126**, 5833-5846 (1999).
28. Orr, B.O., Fetter, R.D. & Davis, G.W. Activation and expansion of presynaptic signaling foci drives presynaptic homeostatic plasticity. *Neuron* **110**, 3743-3759.e3746 (2022).
29. Tsai, P.I. *et al.* Activity-dependent retrograde laminin A signaling regulates synapse growth at *Drosophila* neuromuscular junctions. *Proc Natl Acad Sci U S A* **109**, 17699-17704 (2012).
30. Wang, Q., Han, T.H., Nguyen, P., Jarnik, M. & Serpe, M. Tenectin recruits integrin to stabilize bouton architecture and regulate vesicle release at the *Drosophila* neuromuscular junction. *Elife* **7** (2018).
31. Dani, N., Zhu, H. & Broadie, K. Two protein N-acetylgalactosaminyl transferases regulate synaptic plasticity by activity-dependent regulation of integrin signaling. *J Neurosci* **34**, 13047-13065 (2014).
32. Lee, J.Y., Geng, J., Lee, J., Wang, A.R. & Chang, K.T. Activity-Induced Synaptic Structural Modifications by an Activator of Integrin Signaling at the *Drosophila* Neuromuscular Junction. *J Neurosci* **37**, 3246-3263 (2017).
33. Bloor, J.W. & Kiehart, D.P. zipper Nonmuscle myosin-II functions downstream of PS2 integrin in *Drosophila* myogenesis and is necessary for myofibril formation. *Dev Biol* **239**, 215-228 (2001).
34. Shaner, N.C. *et al.* A bright monomeric green fluorescent protein derived from *Branchiostoma lanceolatum*. *Nature Methods* **10**, 407-409 (2013).
35. Brand, A.H. & Perrimon, N. Targeted gene expression as a means of altering cell fates and generating dominant phenotypes. *Development* **118**, 401-415 (1993).
36. Potter, C.J., Tasic, B., Russler, E.V., Liang, L. & Luo, L. The Q system: a repressible binary system for transgene expression, lineage tracing, and mosaic analysis. *Cell* **141**, 536-548 (2010).
37. Arganda-Carreras, I. *et al.* Trainable Weka Segmentation: a machine learning tool for microscopy pixel classification. *Bioinformatics* **33**, 2424-2426 (2017).
38. Schindelin, J. *et al.* Fiji: an open-source platform for biological-image analysis. *Nature Methods* **9**, 676-682 (2012).
39. Riedl, J. *et al.* Lifeact: a versatile marker to visualize F-actin. *Nature Methods* **5**, 605-607 (2008).
40. Bindels, D.S. *et al.* mScarlet: a bright monomeric red fluorescent protein for cellular imaging. *Nat Methods* **14**, 53-56 (2017).
41. Pollard, T.D. Actin and Actin-Binding Proteins. *Cold Spring Harb Perspect Biol* **8** (2016).
42. Wen, P.J. *et al.* Actin dynamics provides membrane tension to merge fusing vesicles into the plasma membrane. *Nat Commun* **7**, 12604 (2016).
43. Alioto, S.L., Garabedian, M.V., Bellavance, D.R. & Goode, B.L. Tropomyosin and Profilin Cooperate to Promote Formin-Mediated Actin Nucleation and Drive Yeast Actin Cable Assembly. *Curr Biol* **26**, 3230-3237 (2016).
44. Tojkander, S. *et al.* A Molecular Pathway for Myosin II Recruitment to Stress Fibers. *Current Biology* **21**, 539-550 (2011).

45. Abouelezz, A. *et al.* Tropomyosin Tpm3.1 Is Required to Maintain the Structure and Function of the Axon Initial Segment. *iScience* **23**, 101053 (2020).
46. Brettle, M., Patel, S. & Fath, T. Tropomyosins in the healthy and diseased nervous system. *Brain Research Bulletin* **126**, 311-323 (2016).
47. Cho, A., Kato, M., Whitwam, T., Kim, J.H. & Montell, D.J. An Atypical Tropomyosin in *Drosophila* with Intermediate Filament-like Properties. *Cell Rep* **16**, 928-938 (2016).
48. Royou, A., Field, C., Sisson, J.C., Sullivan, W. & Karess, R. Reassessing the role and dynamics of nonmuscle myosin II during furrow formation in early *Drosophila* embryos. *Mol Biol Cell* **15**, 838-850 (2004).
49. Ataman, B., Budnik, V. & Thomas, U. Scaffolding proteins at the *Drosophila* neuromuscular junction. *Int Rev Neurobiol* **75**, 181-216 (2006).
50. Yuan, L., Fairchild, M.J., Perkins, A.D. & Tanentzapf, G. Analysis of integrin turnover in fly myotendinous junctions. *J Cell Sci* **123**, 939-946 (2010).
51. Kechagia, J.Z., Ivaska, J. & Roca-Cusachs, P. Integrins as biomechanical sensors of the microenvironment. *Nat Rev Mol Cell Biol* **20**, 457-473 (2019).
52. Feng, Y., Ueda, A. & Wu, C.F. A modified minimal hemolymph-like solution, HL3.1, for physiological recordings at the neuromuscular junctions of normal and mutant *Drosophila* larvae. *J Neurogenet* **18**, 377-402 (2004).
53. Chighizola, M. *et al.* Mechanotransduction in neuronal cell development and functioning. *Biophys Rev* **11**, 701-720 (2019).
54. Leterrier, C. A Pictorial History of the Neuronal Cytoskeleton. *J Neurosci* **41**, 11-27 (2021).
55. Moseley, J.B. & Goode, B.L. The yeast actin cytoskeleton: from cellular function to biochemical mechanism. *Microbiol Mol Biol Rev* **70**, 605-645 (2006).
56. Tojkander, S., Gateva, G., Husain, A., Krishnan, R. & Lappalainen, P. Generation of contractile actomyosin bundles depends on mechanosensitive actin filament assembly and disassembly. *eLife* **4**, e06126 (2015).
57. Goult, B.T., Yan, J. & Schwartz, M.A. Talin as a mechanosensitive signaling hub. *J Cell Biol* **217**, 3776-3784 (2018).
58. Schiller, H.B. & Fässler, R. Mechanosensitivity and compositional dynamics of cell-matrix adhesions. *EMBO Rep* **14**, 509-519 (2013).
59. Shattil, S.J., Kim, C. & Ginsberg, M.H. The final steps of integrin activation: the end game. *Nat Rev Mol Cell Biol* **11**, 288-300 (2010).
60. Chen, W., Lou, J., Evans, E.A. & Zhu, C. Observing force-regulated conformational changes and ligand dissociation from a single integrin on cells. *J Cell Biol* **199**, 497-512 (2012).
61. Moreno-Layseca, P., Icha, J., Hamidi, H. & Ivaska, J. Integrin trafficking in cells and tissues. *Nat Cell Biol* **21**, 122-132 (2019).
62. Humphries, J.D., Byron, A. & Humphries, M.J. Integrin ligands at a glance. *J Cell Sci* **119**, 3901-3903 (2006).
63. Swaminathan, V. *et al.* Actin retrograde flow actively aligns and orients ligand-engaged integrins in focal adhesions. *Proc Natl Acad Sci U S A* **114**, 10648-10653 (2017).
64. Dubey, S. *et al.* The axonal actin-spectrin lattice acts as a tension buffering shock absorber. *eLife* **9**, e51772 (2020).
65. D'Este, E., Kamin, D., Göttfert, F., El-Hady, A. & Hell, S.W. STED nanoscopy reveals the ubiquity of subcortical cytoskeleton periodicity in living neurons. *Cell Rep* **10**, 1246-1251 (2015).
66. Unsain, N. *et al.* Remodeling of the Actin/Spectrin Membrane-associated Periodic Skeleton, Growth Cone Collapse and F-Actin Decrease during Axonal Degeneration. *Sci Rep* **8**, 3007 (2018).
67. Sood, P. *et al.* Cargo crowding at actin-rich regions along axons causes local traffic jams. *Traffic* **19**, 166-181 (2018).
68. Nishimura, Y. *et al.* The formin inhibitor SMIFH2 inhibits members of the myosin superfamily. *J Cell Sci* **134** (2021).
69. Mutalik, S.P., Joseph, J., Pullarkat, P.A. & Ghose, A. Cytoskeletal Mechanisms of Axonal Contractility. *Biophys J* **115**, 713-724 (2018).
70. Schneider, F., Metz, I. & Rust, M.B. Regulation of actin filament assembly and disassembly in growth cone motility and axon guidance. *Brain Res Bull* **192**, 21-35 (2023).
71. Wang, G. *et al.* Structural plasticity of actin-spectrin membrane skeleton and functional role of actin and spectrin in axon degeneration. *Elife* **8** (2019).
72. Ermanoska, B. *et al.* Tyrosyl-tRNA synthetase has a noncanonical function in actin bundling. *Nat Commun* **14**, 999 (2023).

Non-muscle myosin II regulates presynaptic actin assemblies and neuronal mechanobiology

Supplementary information

This supplementary information file includes:

Supplementary Figures 1 to 6

References for the supplementary information

Source data table

Table 1

Other supplementary materials for this manuscript include the following:

Supplementary Movies 1-10

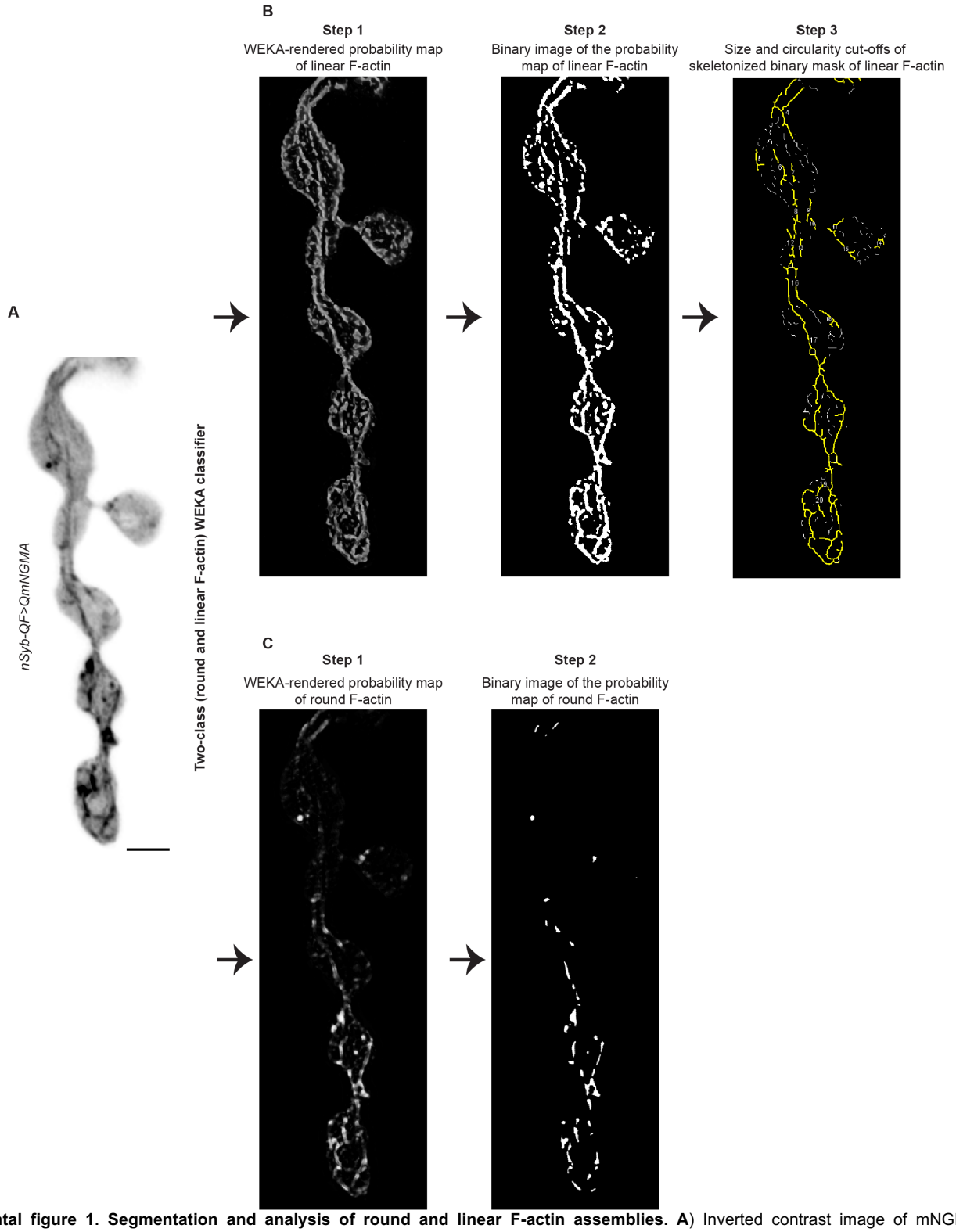

Supplemental figure 1. Segmentation and analysis of round and linear F-actin assemblies. A) Inverted contrast image of mNGMA-labeled presynaptic actin in live dissected larvae as an example for the image analysis pipeline. A two-class (round and linear F-actin) WEKA classifier was applied. **B**) The product of the WEKA-based segmentation of linear actin is a 32-bit probability map image, which is converted to 16-bit image to make a binary mask (8-bit). The binary mask was further skeletonized, and a circularity (0-0.2) and size (0.02 μm^2-Infinity) cutoffs were implemented at the particle analysis step to distinguish *bona fide* linear F-actin. **C**) The 32-bit probability map image of round F-actin was similarly converted to 16-bit image, which was used to make a binary mask of the structures. The binary mask was used in particle analysis of structures with size higher than 0.0018 μm^2. See additional description in Methods.

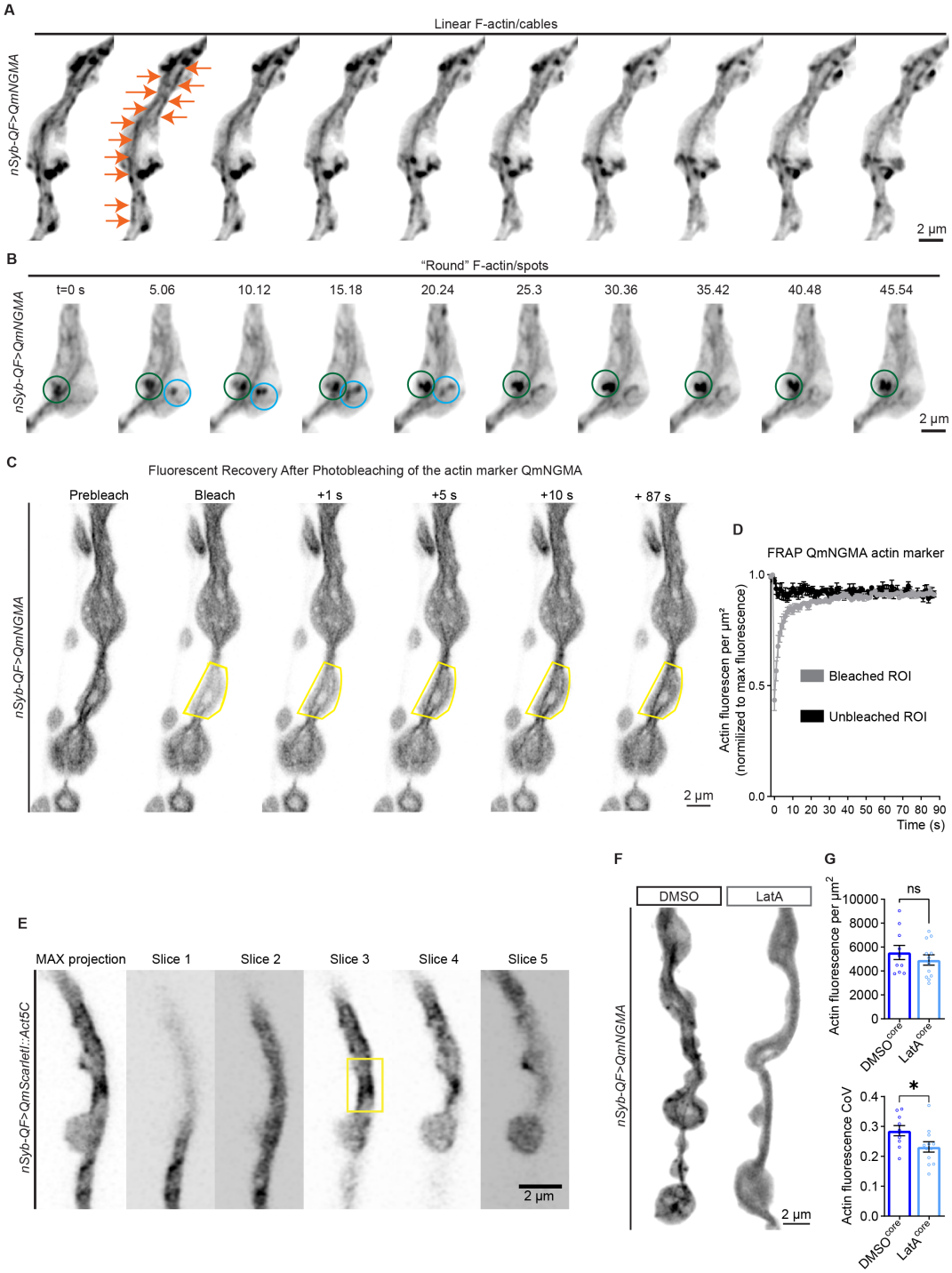

Supplemental Figure 2. Presynaptic actin cytoskeleton at the larval *Drosophila* neuromuscular junction. A) Time-lapse insets (from Supp. movie 1) showing the structure and lifetime of linear F-actin/cable-like structures at the NMJ. **B**) Time-lapse insets of round presynaptic F-actin assemblies (encircled) with different lifetimes (green circle around a longer-lived assembly, light-blue circle around a short-lived, possibly endocytic event) visualized via the actin marker QmNGMA at the NMJ. **C**) Time-lapse of a fluorescence recovery after photobleaching (FRAP) of the neuronally expressed actin marker QmNGMA at a bouton containing linear F-actin assemblies. The bleached bouton is outlined in yellow. **D**) FRAP quantification of linear F-actin-containing region showing recovery of QmNGMA (1 frame/sec, n=3). **E**) Inverted contrast montage of the maximum intensity projection, along with individual Z-stacks of an NMJ from a larvae expressing mScarlet-I::Act5C neuronally (*nSybQF>mScarI::Act5C*). The yellow rectangle marks a typical region of the NMJ selected for FRAP analysis of the presynaptic actin core. **F**) Presynaptic actin assemblies are sensitive to a treatment with the actin depolymerization-inducing drug Latrunculin A (LatA). **G**) Quantifications of the fluorescence per μm^2 and coefficient of variation (CoV) for the QmNGMA actin marker in DMSO and LatA-treated larval fillets, measured through the middle of NMJs, where the actin core predominantly traverses. Error bars represent SEM. N in bar graphs – NMJs. ns – non-significant, * $p<0.05$, ** $p<0.01$, and *** $p<0.001$ upon unpaired, non-parametric Mann-Whitney test. Scale bars – 2 µm. **See Table 1 for detailed genotypes and N.**

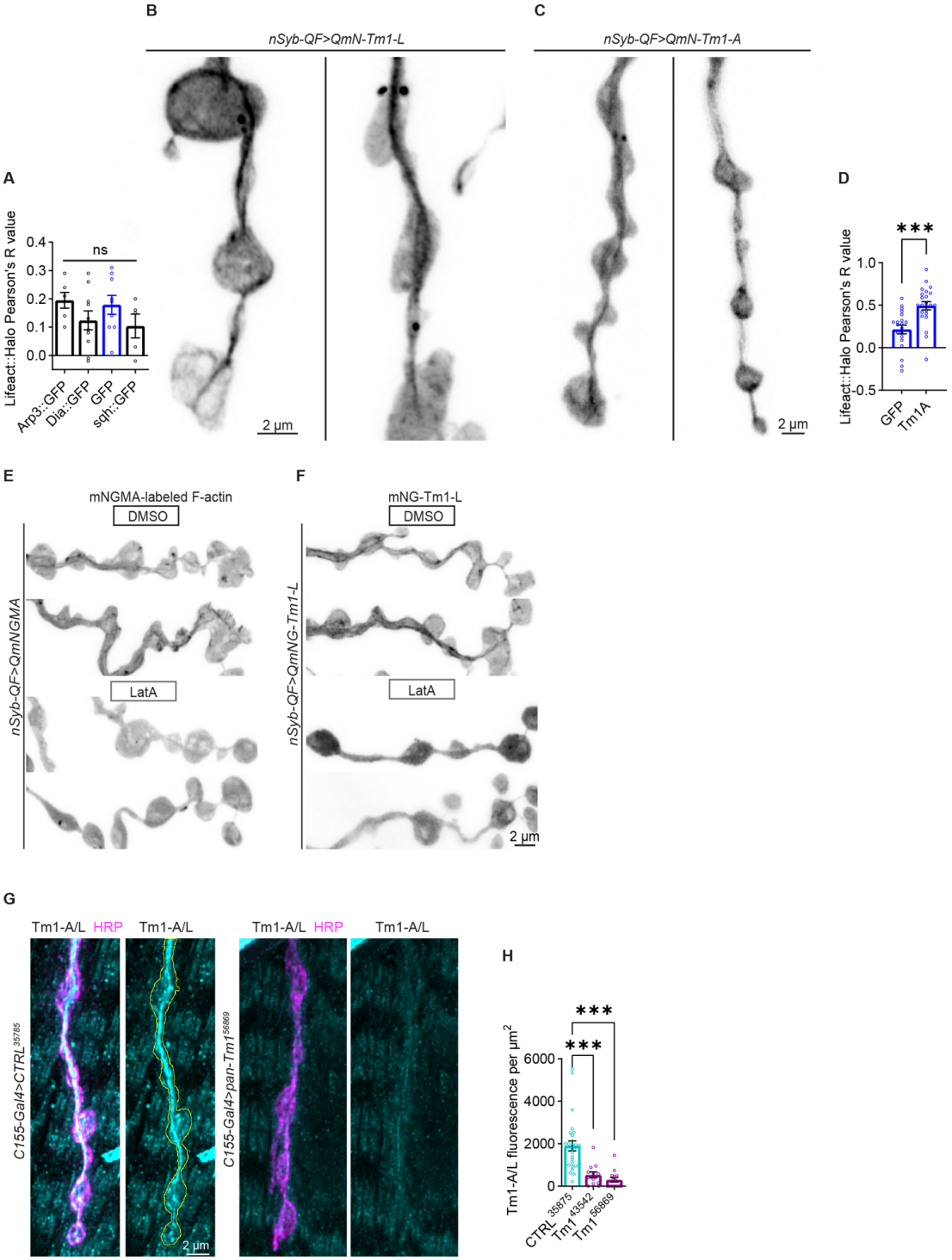

Supplemental Figure 3. Association of actin-binding proteins with linear F-actin structures in the presynaptic core. A) Pearson's R correlation between Lifeact::Halo and Arp3::GFP, Dia::GFP, GFP alone (control), and sqh::GFP (see **Fig. 2**). **B**) Inverted contrast single frame from live imaging depicting the localization pattern upon neuronal expression of mNeonGreen-tagged Tm1-L (mNG-Tm1-L or "long" Tm1) and Tm1-A (mN-Tm1-A or "short" Tm1) in **C**). **D**) Pearson's R correlation between Lifeact::Halo and GFP or mNG-Tm1-A (see Fig. 2C). **E)** The presynaptic localization of mNGMA-labeled actin assemblies and **F**) mNG-Tm1-L is sensitive to treatment with LatA, and not the vehicle DMSO, supporting F-actin-Tm1 association with the presynaptic actin core. **G**) Immunolabeled endogenous Tm1 (cyan) in larvae expressing control RNAi demonstrates that Tm1 traverses along the NMJ (labeled with HRP - magenta) and the antibody used is specific to Tm1, as the signal is depleted upon neuronal expression of Tm1 RNAi, targeting the Tm1 isoforms A, Q and R (*Tm1*^{56869} – note this is a complementary line to pan-Tm1 RNA *Tm1*^{43542} in **Fig. 2E**). **H**) Quantification of the Tm1-A/L fluorescence per µm^2 at NMJs from larvae neuronally expressing *CTRL*, *Tm1*^{43542} or *Tm1*^{56869} RNAi lines. Ns – non-significant, *** p<0.001, and *** p<0.001 upon unpaired, non-parametric Mann-Whitney test. N in bar graphs – NMJs. Error bars are SEM. Scale bars – 2 µm. **See Table 1 for detailed genotypes and N.**

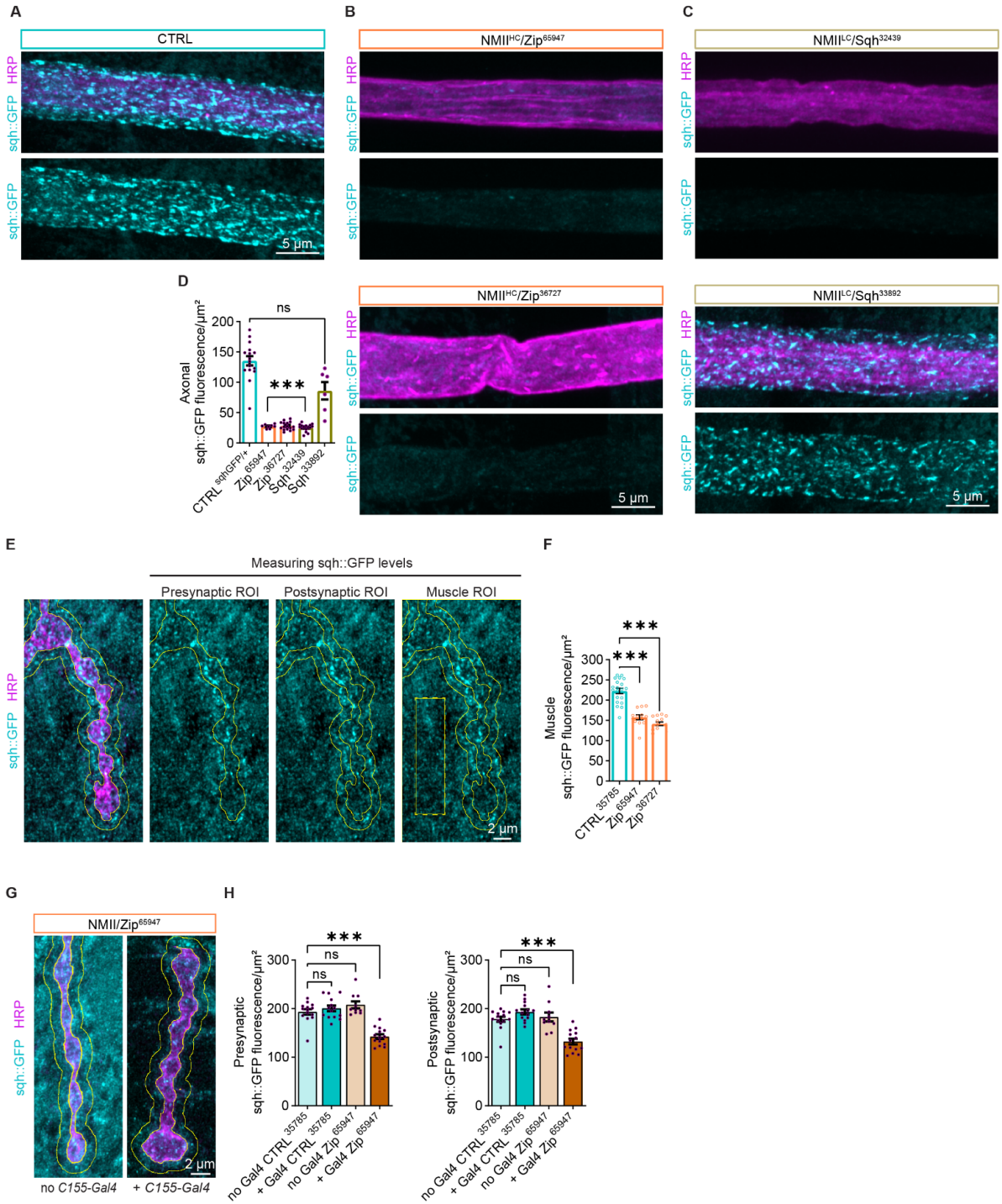

Supplemental figure 4. Validation of *UAS-RNAi* lines targeting NMII^{HC}/Zip and NMII^{LC}/Sqh. A) Distribution of Sqh::GFP (cyan) in axons (labeled with HRP in magenta) proximal to muscle 4 in Sqh::GFP/+ heterozygous larvae. **B**) Neuronal overexpression (*C155-Gal4*) of two independent *UAS-RNAi* lines (*Zip^{65947}* and *Zip^{36727}*) targeting NMII^{HC}/Zip significantly decreases the levels of Sqh::GFP in axons. **C**) Neuronal overexpression of the RNAi line *Sqh^{32439}* significantly decreases the levels of Sqh::GFP in axons. The independent line *Sqh^{33892}* does not significantly alter Sqh::GFP levels. **D**) Quantification of the Sqh::GFP fluorescence in axons of larvae with the different genotypes shown in the previous panels. **E**) Example of image analysis in Fiji, where the Sqh::GFP fluorescence was measured within the presynaptic terminal (masked by HRP/presynaptic ROI), in a 1 µm rim surrounding the bouton (postsynaptic ROI), and in the muscle ROI (rectangle with yellow dashed lines) (excluding the presynaptic compartment and the surrounding 1 µm rim). **F**) Analysis of the Sqh::GFP fluorescence per µm^2 in muscles of larvae expressing *CTRL-* and *Zip RNAi* lines, measured as shown in panel **E**. **G**) Sqh::GFP at NMJs from larvae carrying *Zip^{65947}* in absence and presence of the neuronal *C155-Gal* driver. H) Quantifications of its presynaptic and postsynaptic fluorescence in an experiment validating the lack of nonspecific expression of *Zip^{65947}* in neurons and muscles in absence of Gal4 driver. Ns – non-significant, *** p<0.001 after One-way ANOVA with Kruskal-Wallis multiple comparison test. N in bar graphs – NMJs. Error bars are SEMs. Scale bars B and C – 5 µm; in E and G – 2 µm. **See Table 1 for detailed genotypes and N.**

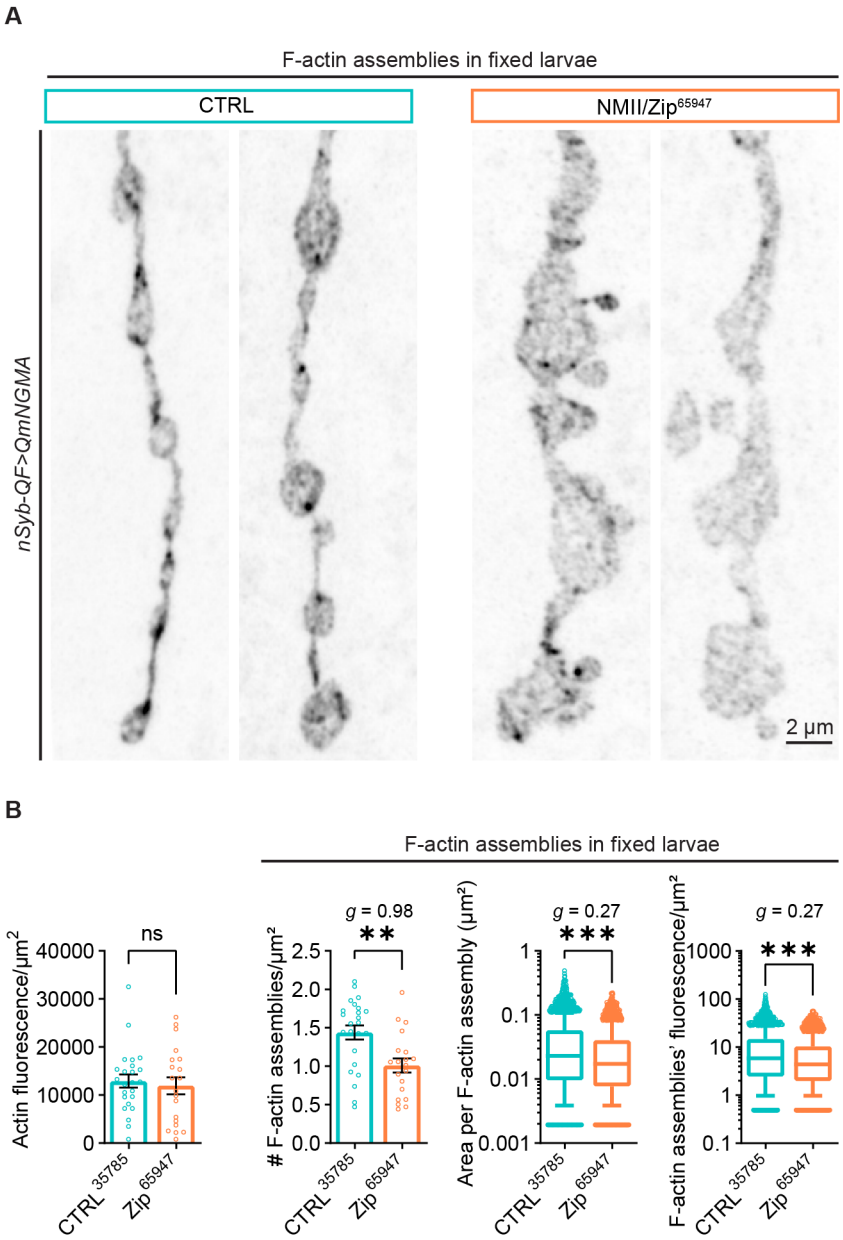

Supplemental figure 5. Presynaptic actin assemblies upon down-regulation of non-muscle Myosin II in neurons. A) Inverted contrast QmNGMA-labeled presynaptic actin in fixed larvae co-expressing *CTRL*- or *NMII/Zip*^{65947} RNAi lines. **B**) Quantification of the fluorescence per µm^2 for the QmNGMA actin marker in whole NMJs, along with the number of actin assemblies per µm^2, and the area and fluorescence intensity of the individual presynaptic actin structure. The actin particles were analyzed without specifying their morphological features as round or linear to account for fragmentation of the presynaptic cytoskeleton as a result of fixation[1]. Box and whiskers graphs were used to represent the results of the area and fluorescence intensity of the individual presynaptic actin structures. Whiskers represent 10th to 90th percentile, while the rest of the data points are shown as individual values. The Y-axis in these graphs represents log10, to capture the broad distribution of the individual values. In bar graphs with linear Y-axis, error bars represent SEM. N in bar graphs – NMJs; N in box and whiskers – individual actin assemblies. Ns – non-significant, ** p<0.01, *** p<0.001 upon unpaired, non-parametric Mann-Whitney test. *g* – Hedges' *g* represents effect size. Scale bar – 2 µm.

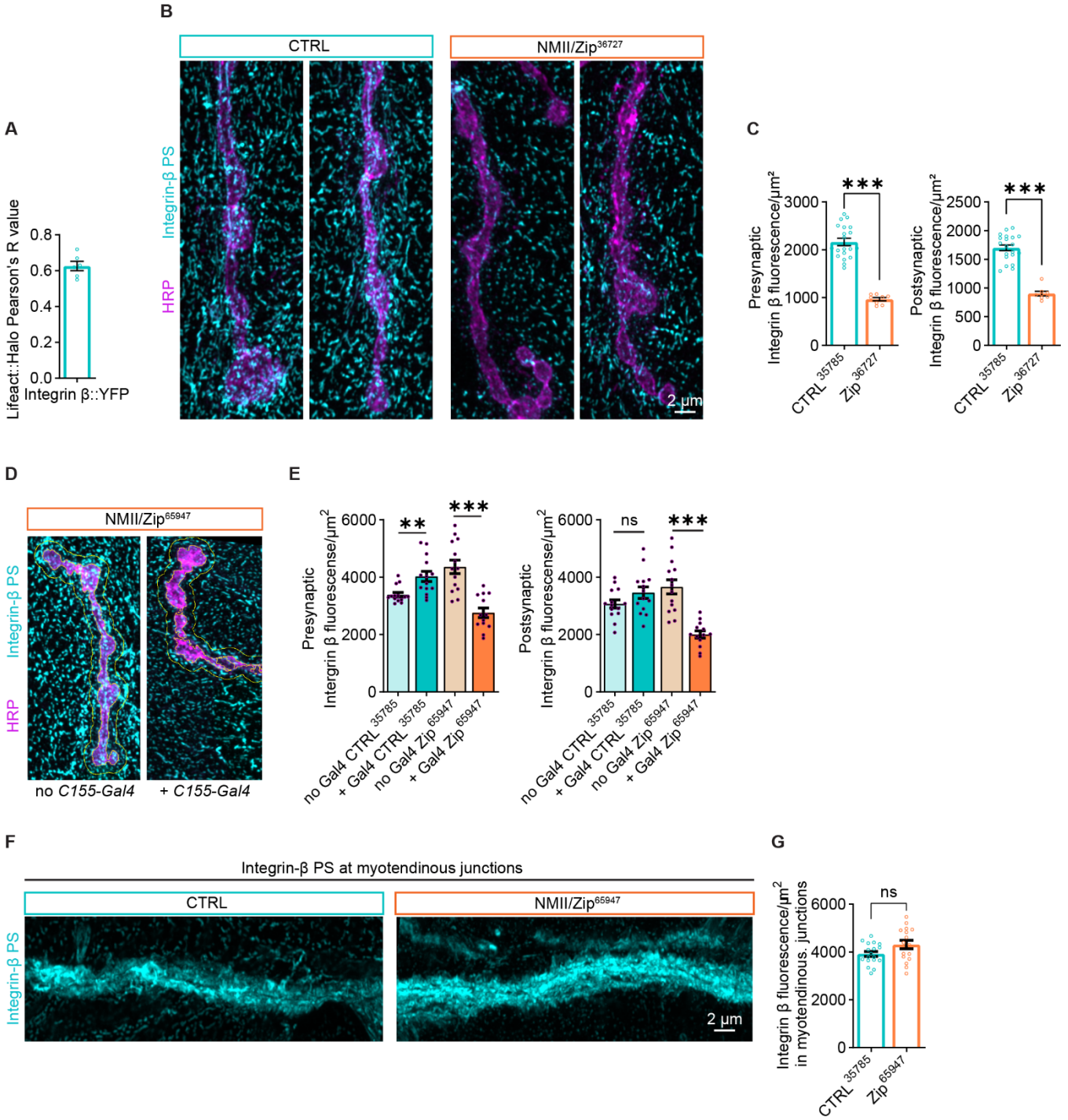

Supplemental Figure 6. Neuronal depletion of non-muscle Myosin II and Tm1 rearranges integrin receptors at the NMJ. A) Pearson's R correlation between Lifeact::Halo and Integrin-β::YFP at NMJs of live larvae. **B**) Reorganization of Integrin-β at NMJs of larvae expressing an independent RNAi line *NMII/Zip*^{36727} in neurons, compared to controls. **C**) Fluorescence intensity per µm^2 of pre- and postsynaptic Integrin-β in control and larvae expressing the independent *Zip*^{36727}. **D**) Integrin-β PS immunofluorescence at NMJs in larvae carrying *Zip*^{65947} in absence and presence of *C155-Gal4* driver. **E**) Quantification of the fluorescence intensity per µm^2 of pre- and postsynaptic Integrin-β in larvae carrying the *CTRL*- and *Zip*^{65947} RNAi lines, in absence and presence of *C155-Gal4*. **F**) Integrin-β PS immunofluorescence at myotendinous junctions of larvae expressing *CTRL*- and *Zip*^{65947} in neurons. **G**) Quantification of the fluorescence per µm^2 of Integrin-β in myotendinous junctions in *CTRL*- and *Zip*^{65947}-expressing larvae (*C155-Gal4>RNAi*). Ns – non-significant, ** p<0.01, *** p<0.001 upon unpaired, non-parametric Mann-Whitney test. Error bars are SEMs. Scale bar – 2 µm.

Legends for the supplementary movies 1-10:

Supplementary Movie S1. Time-lapse movie showing QmNGMA-labeled presynaptic F-actin structures at the NMJ. Each frame is a maximum intensity projection of Z-stacks of presynaptic terminals imaged at a sampling frequency of 1 frame/5 sec. The movie is played at a speed of 2 frames per second. Scale bar – 2 µm.

Supplementary Movie S2. Time-lapse movie of Arp3::GFP (cyan) and the F-actin marker Lifeact::Halo (magenta) at the NMJ. Frames represent maximum intensity projections of Z-stacks of presynaptic terminals imaged at a sampling frequency of 1 frame/2.16 s. The movie is played at a speed of 5 frames per second. Scale bar – 2 µm.

Supplementary Movie S3. Time-lapse movie of Dia::GFP (cyan) and the F-actin marker Lifeact::Halo (magenta) at the NMJ. Frames represent maximum intensity projections of Z-stacks of presynaptic terminals imaged at a sampling frequency of 1 frame/1.3 s. The movie is played at a speed of 5 frames per second. Scale bar – 2 µm.

Supplementary Movie S4. Time-lapse movie of GFP (cyan) and the F-actin marker Lifeact::Halo (magenta) at the NMJ. Frames represent maximum intensity projections of Z-stacks of presynaptic terminals imaged with 1/13.32 s sampling frequency. The movie is played at a speed of 1 frame per second. Scale bar – 2 µm.

Supplementary Movie S5. Time-lapse movie of sqh::GFP(cyan) and the F-actin marker Lifeact::Halo (magenta) at the NMJ. Frames represent maximum intensity projections of Z-stacks of presynaptic terminals imaged at a sampling frequency of 1 frame/13.38 s. The movie is played at a speed of 1 frame per second. Scale bar – 2 µm.

Supplementary Movie S6. Time-lapse movie showing QmNGMA-labeled presynaptic F-actin structures at the NMJ in larvae expressing *CTRL* RNAi in neurons. Frames represent maximum intensity projections of Z-stacks of presynaptic terminals imaged at a sampling frequency of with 1 frame/5 s. The movie is played at a speed of 1 frame per second. Scale bar – 2 µm.

Supplementary Movie S7. Time-lapse movie showing QmNGMA-labeled presynaptic F-actin structures at the NMJ in larvae expressing Zip^{65947} RNAi in neurons. Frames represent maximum intensity projections of Z-stacks of presynaptic terminals imaged at a sampling frequency of 1 frame/5 s. The movie is played at a speed of 1 frame per second. Scale bar – 2 µm.

Supplementary Movie S8. Ventral (muscle proximal) to dorsal (muscle distal) Z-stack played as a movie showing ubiquitously expressed Integrin-β (cyan) and the F-actin marker Lifeact::Halo (magenta) through an NMJ. Scale bar – 2 µm.

Supplementary Movie S9. Time-lapse movie showing QmNGMA-labeled presynaptic F-actin structures at the NMJ in larvae with intact brain and axons. Frames represent maximum intensity projections of Z-stacks of presynaptic terminals imaged at a sampling frequency of 1 frame/1.93 s. The movie is played at a speed of 5 frames per second speed. Scale bar – 2 µm.

Supplementary Movie S10. Time-lapse movie showing QmNGMA-labeled presynaptic F-actin structures at the NMJ in larvae with severed brain and axons. Frames represent maximum intensity projections of Z-stacks of presynaptic terminals imaged at a sampling frequency of 1 frame/1.93 s. The movie is played at a speed of 5 frames per second. Scale bar – 2 µm.

Supplementary reference:

1. Pereira, P.M. *et al.* Fix Your Membrane Receptor Imaging: Actin Cytoskeleton and CD4 Membrane Organization Disruption by Chemical Fixation. *Front Immunol* **10**, 675 (2019).

Source Data Table

REAGENT or RESOURCE	SOURCE	IDENTIFIER
Antibodies		
FluoTag®-X4 anti-GFP (1:250)	NanoTag Biotechnologies	N0304
Rabbit anti-Tm1A/L (1:500)	Denise Montel, University of California, Santa Barbara	NA
Mouse anti-Integrin betaPS (1:50)	Developmental studies hybridoma bank	Cat# cf.6g11
Rhodamine Red™-X (RRX) AffiniPure Goat Anti-Horseradish Peroxidase (1:500)		123-295-021
Chemicals, peptides and recombinant proteins		
DMSO		
InSolution Latrunculin A	Sigma	428026
Janelia Fluor® HaloTag® Ligand-549	Promega	GA111A
Experimental models: Organisms/strains		
D. melanogaster QUAS-mNeonGreen::GMA	This paper	NA
D. melanogaster QUAS-mScarlet-I::Act5C	This paper	NA
D. melanogaster QUAS-Tm1-A	This paper	NA
D. melanogaster QUAS-Tm1-L	This paper	NA
D. melanogaster UAS-Lifeact::Halo2	BDSC	Stock#: 67625
D. melanogasterUAS-Arp3::GFP	BDSC	Stock#: 39723
D. melanogaster UAS-Dia::GFP	BDSC	Stock#: 56751
D. melanogaster UAS-GFP	Leslie Griffith, Brandeis University	
D. melanogaster UAS-CTRL-RNAi35785	BDSC	Stock#: *35785*
D. melanogaster UAS-Zip-RNAi65947	BDSC	Stock#: *65947*
D. melanogaster UAS-Zip-RNAi32727	BDSC	Stock#: *32727*
D. melanogaster UAS-Sqh-RNAi32439	BDSC	Stock#: *32439*
D. melanogaster UAS-Sqh-RNAi33892	BDSC	Stock#: *33892*
D. melanogaster sqh::GFP	BDSC	Stock#: 57145
D. melanogaster P{Ubi-mys.YFP}	Guy Tanentzapf, University of British Columbia	Yuan et al., 2010
D. melanogaster C155-Gal4		
D. melanogaster nSyb-QF2		
Software and algorithms		
Fiji		
GraphPad Prism		

References:

1. Bloor, J.W. & Kiehart, D.P. zipper Nonmuscle myosin-II functions downstream of PS2 integrin in Drosophila myogenesis and is necessary for myofibril formation. *Dev Biol* **239**, 215-228 (2001).
2. Feng, Y., Ueda, A. & Wu, C.F. A modified minimal hemolymph-like solution, HL3.1, for physiological recordings at the neuromuscular junctions of normal and mutant Drosophila larvae. *J Neurogenet* **18**, 377-402 (2004).
3. Schindelin, J. *et al.* Fiji: an open-source platform for biological-image analysis. *Nature Methods* **9**, 676-682 (2012).
4. Arganda-Carreras, I. *et al.* Trainable Weka Segmentation: a machine learning tool for microscopy pixel classification. *Bioinformatics* **33**, 2424-2426 (2017).

Table 1. Experimental genotype and statistical reporting.

Figure	Genotype/Conditions	N	Measurement	Statistical Test(s)
Figure 1	**Fig. 1. Presynaptic actin cytoskeleton at the *Drosophila* larval NMJ.**			
Fig. 1A	Diagram of the *Drosophila* larval neuromuscular system as a tissue mechanics model.			
Fig. 1B: A single frame from live imaging (See also **Supp. Movie S1**) of presynaptic actin assemblies visualized via neuronal expression of the genetically encoded actin marker mNeonGreen-GMA (mNGMA) in larval preparations with intact brains.	*C155-Gal4/Y; QUAS-mNeonGreenMA(GMA)/+; nSyb-QF2/+*			
Fig. 1C: A single frame from live imaging of NMJs expressing an independent genetically encoded actin marker Lifeact::Halo delineates similar spot-like and cable-like (core) actin assemblies.	*C155-Gal4/Y;UAS-Lifeact//Halo:+*			
Fig. 1D: A single frame from live imaging of the *Drosophila* actin isoform 5C, tagged with the red fluorescent protein mScarlet-I (QAct5C::mScarI), similarly delineates the actin core in addition to round F-actin assemblies.	*C155-Gal4/Y; QUAS-Act5C::mScarI/+; nSyb-QF2/+*	9 larva/ 16 NMJs		
Fig. 1E: Image sequences of FRAP of QAct5C::mScarI-labeled actin core.	*C155-Gal4/Y; QUAS-Act5C::mScarI/+; nSyb-QF2/+*	9 larva/ 16 NMJs		
Fig. 1F: FRAP curve of QAct5C::mScarI **BE114**	*C155-Gal4/Y; QUAS-Act5C::mScarI/+; nSyb-QF2/+*	9 larva/ 16 NMJs	Actin fluorescence per μm^2	None.
Figure 2.	**Fig. 2. Molecular composition of linear F-actin structures at the presynaptic core.**			
Fig. 2A: The branched actin network nucleator Arp2/3, visualized via Arp3::GFP (cyan), decorates spot-like and linear F-actin assemblies labeled with Lifeact::Halo (magenta). See also **Supp. Movie S2**.	*C155-Gal4/Y; UAS-Arp3::GFP/UAS-Lifeact::Halo*			
Fig. 2B: The nucleator of linear actin assemblies formin/Dia::GFP (cyan) decorates actin cables (magenta). See also **Supp. Movie S3**.	*C155-Gal4/Y;UAS-Dia::EGFP/UAS-Lifeact::Halo*			
Fig. 2C: Diffuse cytosolic GFP (cyan) shows no specific enrichment or co-localization with presynaptic actin assemblies (magenta). See also **Supp. Movie S4**.	*C155-Gal4/Y;UAS-GFP/UAS-Lifeact::Halo*			

Fig. 2D: The F-actin stabilizer Tm1-A is enriched in the linear Lifeact::Halo-marked actin assemblies along the presynaptic core.	*C155-Gal4/Y; UAS-Lifeact::Halo/QUAS-mNeonGreenTm1-A; nSyb-QF2/+*	8 larvae/ 23 NMJs		
Fig. 2E Endogenous Tm1 in larvae expressing control RNAi and *panTm1*^{43542} in neurons.	*C155-Gal4/Y;; UAS-CTRL*^{35785}*/+* *C155-Gal4/Y;; UAS-panTm1*^{43542}*/+*	8 larvae/28 NMJs 5 larvae/13 NMJs		
Fig. 2E: Distribution of the non-muscle myosin II light chain subunit sqh::GFP at the NMJ in live larvae expressing Lifeact::Halo in neurons. See also **Supp. Movie S5**.	*C155-Gal4/Y; UAS-Lifeact::Halo/+; sqh::GFP/+*			
Figure 3.	**Fig. 3. Non-muscle Myosin II regulates the integrity of presynaptic actin assemblies.**			
Fig. 3A: mNGMA-labeled presynaptic actin in larvae co-expressing *CTRL RNAi* line. See also **Supp. Movie S6**.	*C155-Gal4/Y; QUAS-mNeonGreenMA(GMA)/UAS-CTRL*^{35785}*; nSyb-QF2/+*	8 larva/ 23 NMJs		
Fig. 3B: mNGMA-labeled presynaptic actin in larvae co-expressing *NMII/Zip*^{65947} RNAi lines. See also **Supp. Movie S7**.	*C155-Gal4/Y; QUAS-mNeonGreenMA(GMA)/UAS-Zip*^{65947}*; nSyb-QF2/+*	9 larva/ 26 NMJs		
Fig. 3C: Quantification of fluorescence per µm^2 for the QmNGMA actin marker in whole NMJs.	*C155-Gal4/Y;QUAS-mNeonGreenMA(GMA)/UAS-CTRL*^{35785}*; nSyb-QF2/+* *C155-Gal4/Y;QUAS-mNeonGreenMA(GMA)/UAS-Zip*^{65947}*; nSyb-QF2/+*	8 larva/ 23 NMJs 9 larva/ 26 NMJs	Actin fluorescence per µm^2	Error bars represent SEM. ns – not significant, upon unpaired, non-parametric Mann-Whitney test. N – number of NMJs
Fig. 3D: Quantifications of the number of round F-actin assemblies per µm^2, as well as the area and fluorescence of the individual round presynaptic actin structures.	*C155-Gal4/Y; QUAS-mNeonGreenMA(GMA)/UAS-CTRL*^{35785}*; nSyb-QF2/+* *C155-Gal4/Y; QUAS-mNeonGreenMA(GMA)/UAS-Zip*^{65947}*; nSyb-QF2/+*	8 larva/ 23 NMJs 9 larva/ 26 NMJs	Number of spot-like F-actin assemblies per µm^2	Error bars represent SEM. ns – not significant, * $p<0.05$, upon unpaired, non-parametric Mann-Whitney test. N – number of NMJs
		8 larva/ 23 NMJs/976 actin spots (N) 9 larva/ 26 NMJs/1010 actin spots (N)	Area of individual spot-like presynaptic actin structures (µm^2)	ns – not significant, upon unpaired, non-parametric Mann-Whitney test. N – number of individual spots
		8 larva/ 23 NMJs/976 actin spots (N)	Fluorescence per µm^2 of individual spot-like presynaptic actin structures	ns – not significant, upon unpaired, non-parametric Mann-Whitney test. N – number of individual spots

		9 larva/ 26 NMJs/1010 actin spots (N)		
Fig. 3E: Graphs representing the percentage of NMJ area covered with linear F-actin, as well as the area and fluorescence of the individual assemblies.	*C155-Gal4/Y; QUAS-mNeonGreenMA(GMA)/UAS-CTRL^{35785}; nSyb-QF2/+* *C155-Gal4/Y; QUAS-mNeonGreenMA(GMA)/UAS-Zip^{65947}; nSyb-QF2/+*	8 larva/ 23 NMJs 9 larva/ 26 NMJs	Percentage of the NMJ area covered with linear F-actin assemblies	Error bars represent SEM. ns – not significant, ** p<0.01, *** p<0.001, upon unpaired, non-parametric Mann-Whitney test. N – number of NMJs
		8 larva/ 23 NMJs/519 structures 9 larva/ 26 NMJs/821 structures	Area of individual linear presynaptic actin structures (μm^2)	Error bars represent SEM. ns – not significant, ** p<0.01, upon unpaired, non-parametric Mann-Whitney test. N – number of linear actin structures
		8 larva/ 23 NMJs/519 linear assemblies (N) 9 larva/ 26 NMJs/821 linear assemblies (N)	Fluorescence per μm^2 of individual linear presynaptic actin structures	Error bars represent SEM. ns – not significant, ** p<0.01, upon unpaired, non-parametric Mann-Whitney test. N – number of linear actin structures
Figure 4.	**Figure 4. Depletion of Neuronal NMII reduces the levels of the motor in the muscle.**			
Fig. 4A: Sqh::GFP-labeled NMII at NMJs in fixed larvae expressing *CTRL^{35785}*, *Zip^{65947}*, and *Zip^{36727}* RNAi in neurons (*C155-Gal4*).	*C155-Gal4/Y;; sqh::GFP/UAS-CTRL^{35785}* *C155-Gal4/Y;; sqh::GFP/UAS-Zip^{65947}* *C155-Gal4/Y;; sqh::GFP/UAS-Zip^{36727}*			
Fig. 4B: Analysis of the presynaptic Sqh::GFP fluorescence per μm^2, as well as the number, area and fluorescence of WEKA-segmented individual sqh::GFP particles.	*C155-Gal4/Y;; sqh::GFP/UAS-CTRL^{35785}* *C155-Gal4/Y;; sqh::GFP/UAS-Zip^{65947}* *C155-Gal4/Y;; sqh::GFP/UAS-Zip^{36727}*	10 larvae/ 20 NMJs 7 larvae/ 15 NMJs 7 larvae/ 14 NMJs	Presynaptic sqh::GFP fluorescence per μm^2	** p<0.01, *** p<0.001 after one-way ANOVA with Šídák's multiple comparisons test.
		10 larvae/ 20 NMJs 7 larvae/ 15 NMJs	Number of presynaptic sqh::GFP particles per μm^2	

		7 larvae/ 14 NMJs		
		10 larvae/ 20 NMJs/ 11360 particles (N) 7 larvae/ 15 NMJs/5544 (N) 7 larvae/ 14 NMJs/5007 (N)	Area of individual presynaptic sqh::GFP particles (μm^2)	
		10 larvae/ 20 NMJs/ 11360 particles (N) 7 larvae/ 15 NMJs/5544 (N) 7 larvae/ 14 NMJs/5007 (N)	sqh::GFP fluorescence per μm^2 in individual presynaptic particles	
Fig. 4C: Analysis of the postsynaptic Sqh::GFP fluorescence per μm^2, as well as the number, area and fluorescence of WEKA-segmented individual sqh::GFP particles.	*C155-Gal4/Y;; sqh::GFP/UAS-CTRL*^{35785} *C155-Gal4/Y;; sqh::GFP/UAS-Zip*^{65947} *C155-Gal4/Y;; sqh::GFP/UAS-Zip*^{36727}	10 larvae/ 20 NMJs 7 larvae/ 15 NMJs 7 larvae/ 14 NMJs	Postsynaptic sqh::GFP fluorescence per μm^2	** $p<0.01$, *** $p<0.001$ after one-way ANOVA with Šídák's multiple comparisons test.
		10 larvae/ 20 NMJs 7 larvae/ 15 NMJs 7 larvae/ 14 NMJs	Number of postsynaptic sqh::GFP spots per μm^2	
		10 larvae/ 20 NMJs/20096 particles 7 larvae/ 15 NMJs/9044 particles 7 larvae/ 14 NMJs/ 8916 particles	Area of individual postsynaptic sqh::GFP particles (μm^2)	
		10 larvae/ 20 NMJs/20096 particles 7 larvae/ 15 NMJs/9044 particles	sqh::GFP fluorescence per μm^2 of individual postsynaptic particles	

		7 larvae/ 14 NMJs/ 8916 particles		
Figure 5.	**Fig. 5. Neuronal depletion of non-muscle Myosin II rearranges integrin receptors at the NMJ.**			
Fig. 5A: Distribution of YFP-tagged, ubiquitously expressed Integrin-β (cyan) at NMJs in live larvae expressing Lifeact::Halo (magenta) in neurons. See also **Supp. Movie S8**.	*C155-Gal4/Y;UAS-Lifeact::Halo/+; ubiIntegrin-β PS::YFP/+*			None
Fig. 5B: Immunostaining of Integrin-β (cyan) at NMJs of control larvae.	*C155-Gal4/Y;;UAS-CTRL*^{35785}/+			None
Fig. 5C: Reorganization of Integrin-β at NMJs of larvae expressing *Zip*^{65947} in neurons, compared to controls.	*C155-Gal4/Y;;UAS-CTRL*^{35785}/+	9 larvae/ 18 NMJs		None
	C155-Gal4/Y;;UAS- Zip^{65947}/+	8 larvae/ 16 NMJs		
Fig. 5D: Quantification of Integrin-β in presynaptic linear structures.	*C155-Gal4/Y;;UAS-CTRL*^{35785}/+ *C155-Gal4/Y;;UAS- Zip*^{65947}/+	9 larvae/ 18 NMJs 8 larvae/ 16 NMJs	Percentage of NMJ area covered with linear Integrin-β	* $p<0.05$, ** $p<0.01$, and *** $p<0.001$ upon unpaired, non-parametric Mann-Whitney test.
		9 larvae/ 18 NMJs/485 structures 8 larvae/ 16 NMJs/130 structures	Area of individual linear Integrin-β	
		9 larvae/ 18 NMJs/485 structures 8 larvae/ 16 NMJs/130 structures	Integrin-β fluorescence per μm^2 in individual linear structures	
Fig. 5E: Quantification of Integrin-β in presynaptic foci.	*C155-Gal4/Y;;UAS-CTRL*^{35785}/+ *C155-Gal4/Y;;UAS- Zip*^{65947}/+	9 larvae/ 18 NMJs 8 larvae/ 16 NMJs	Number of presynaptic Integrin-β spots per μm^2	* $p<0.05$, and *** $p<0.001$ upon unpaired, non-parametric Mann-Whitney test.
		9 larvae/ 18 NMJs/4039 spots 8 larvae/ 16 NMJs/1897 spots	Area of individual presynaptic Integrin-β spots (μm^2)	

		9 larvae/ 18 NMJs/4039 spots 8 larvae/ 16 NMJs/1897 spots	Integrin-β fluorescence per μm^2 in individual presynaptic spots	
Fig. 5F: Quantification of Integrin-β in postsynaptic foci.	*C155-Gal4/Y;;UAS-CTRL^{35785}/+* *C155-Gal4/Y;;UAS- Zip^{65947}/+*	9 larvae/ 18 NMJs 8 larvae/ 16 NMJs	Number of postsynaptic Integrin-β spots per μm^2	*** p<0.001 upon unpaired, non-parametric Mann-Whitney test.
		9 larvae/ 18 NMJs/7003 8 larvae/ 16 NMJs/3344	Area of individual postsynaptic Integrin-β spots (μm^2)	
		9 larvae/ 18 NMJs/7003 8 larvae/ 16 NMJs/3344	Integrin-β fluorescence per μm^2 in individual postsynaptic spots	
Figure 6.	**Fig. 6. Mechanical severing of larval axons induces changes in presynaptic F-actin.**			
Fig. 6A: Diagram of *Drosophila* fillet preparation upon axotomy (light blue dashed line) of all proximal neurons descending from the larval brain. This procedure removes the axonal tension exerted at presynaptic compartments.				
Fig. 6B: mNGMA-labeled presynaptic actin at NMJs from live larvae with intact brains (left) or upon severing of the brain/axotomy (right). See also **Supp. Movies S9-10**.	*C155-Gal4/Y;QUAS-mNeonGreenMA(GMA)/+; nSyb-QF2/+*	Intact brains		None
	C155-Gal4/Y;QUAS-mNeonGreenMA(GMA)/+; nSyb-QF2/+	Axotomy		
Fig. 6C: Quantification of the fluorescence per μm^2 for the QmNGMA actin marker in whole NMJs.	*C155-Gal4/Y;QUAS-mNeonGreenMA(GMA)/+; nSyb-QF2/+*	<u>Intact brain:</u> 8 larvae/17 NMJs <u>Axotomy:</u> 8 larvae/17 NMJs	Actin fluorescence per μm^2	ns – not significant, ** p<0.01, and *** p<0.001 upon unpaired, non-parametric Mann-Whitney test.

Fig. 6D: Quantifications of the number of round F-actin assemblies per µm^2, as well as the area and fluorescence of the individual round presynaptic actin structures.	*C155-Gal4/Y;QUAS-mNeonGreenMA(GMA)/+; nSyb-QF2/+*	Intact brain: 8 larvae/17 NMJs Axotomy: 8 larvae/17 NMJs	Number of spot-like F-actin assemblies per µm^2	
		Intact brain: 8 larvae/17 NMJs/400 Axotomy: 8 larvae/17 NMJs/600	Area of individual round F-actin structures (µm^2)	
			Actin fluorescence per µm^2 in individual round F-actin structures	
Fig. 6E: Graphs representing the percentage of NMJ area covered with linear F-actin, as well as the area and fluorescence of the individual assemblies.	*C155-Gal4/Y;QUAS-mNeonGreenMA(GMA)/+; nSyb-QF2/+*	Intact brain: 8 larvae/17 NMJs Axotomy: 8 larvae/17 NMJs	Percentage of the NMJ area covered with linear F-actin assemblies	
		Intact brain: 8 larvae/17 NMJs/123 Axotomy: 8 larvae/17 NMJs/132	Area of individual linear presynaptic actin structures (µm2)	
			Actin fluorescence per µm^2 in individual linear actin structures	
Supplemental figure 1.	**Segmentation and analysis of round and linear F-actin assemblies.**			
Supplemental Figure 2.	**Supplemental Figure 2. Presynaptic actin cytoskeleton at the larval *Drosophila* neuromuscular junction.**			
Supp. Fig.2A: Time-lapse insets (from **Supp. Movie S1**) showing the structure and lifetime of linear F-actin/cable-like structures at the NMJ.	*C155-Gal4/Y;QUAS-mNeonGreenMA(GMA)/+; nSyb-QF2/+*			None
Supp. Fig.2B: Time-lapse insets (from **Supp. Movie S1**) of spot-like presynaptic F-actin assemblies (pointed with green arrows) with different lifetimes (green arrows point a longer-lived assembly, light-blue arrow shows a short-lived, possibly endocytic event) visualized via the actin marker QmNGMA at the NMJ.	*C155-Gal4/Y;QUAS-mNeonGreenMA(GMA)/+; nSyb-QF2/+*			None

Supp. Fig.2C: Time-lapse of a fluorescence recovery after photobleaching (FRAP) of the neuronally expressed actin marker QmNGMA at a bouton containing linear F-actin assemblies. The bleached bouton is outlined in yellow.	*C155-Gal4/Y;QUAS-mNeonGreenMA(GMA)/+; nSyb-QF2/+*			
Supp. Fig.2D: FRAP quantification of linear F-actin-containing region showing recovery of QmNGMA.	*C155-Gal4/Y;QUAS-mNeonGreenMA(GMA)/+; nSyb-QF2/+*		2 larvae/ 5 NMJs	None
Supp. Fig. 2F: Presynaptic actin assemblies are sensitive to a treatment with the actin depolymerization-inducing drug Latrunculin A (LatA).	*C155-Gal4/Y;QUAS-mNeonGreenMA(GMA)/+; nSyb-QF2/+*	**DMSO condition:** 5 larva/ 12 NMJs **LatA treatment:** 6 larva/ 18 NMJs		
Supp. Fig. 2G: Quantifications of the fluorescence per μm^2 and coefficient of variation (CoV) for the QmNGMA actin marker in DMSO and LatA-treated larval fillets, measured through the middle of NMJs, where the actin core predominantly traverses.	*C155-Gal4/Y;QUAS-mNeonGreenMA(GMA)/+; nSyb-QF2/+*	**DMSO condition:** 5 larva/ 12 NMJs **LatA treatment:** 6 larva/ 18 NMJs	Fluorescence per μm^2 and coefficient of variation (CoV) for the QmNGMA actin marker	ns – not significant, * $p<0.05$, ** $p<0.01$, and *** $p<0.001$ upon unpaired, non-parametric Mann-Whitney test.
Supplemental Figure 3.	**Association of actin-binding proteins to linear F-actin structures at the presynaptic core.**			
Supp. Fig. 3A: Pearson's R correlation between Lifeact::Halo and Arp3::GFP, Dia::GFP, GFP alone (control), and sqh::GFP.	*C155-Gal4/Y;UAS-Arp3::GFP/UAS-Lifeact::Halo* *C155-Gal4/Y;UAS-Dia::EGFP/UAS-Lifeact::Halo* *C155-Gal4/Y;UAS-GFP/UAS-Lifeact::Halo* *C155-Gal4/Y;UAS-Lifeact::Halo/+; sqh::GFP/+*	3 larvae/6 NMJs 4 larvae/10 NMJs 3 larvae/9 NMJs 2 larvae/ 6 NMJs	Pearson's R correlation	Ns – non-significant after one-way ANOVA with Šídák's multiple comparisons test. Error bars represent SEM.
Supp. Fig. 3B-C: Inverted contrast single frame from live imaging depicting the localization pattern upon neuronal expression of mNeonGreen-tagged Tm1-L (mNG-Tm1-L or "long" Tm1) and Tm1-A (mN-Tm1-A or "short" Tm1).	*C155-Gal4/Y;QUAS-mNeonGreen::Tm1-L/+; nSyb-QF2/+* *C155-Gal4/Y;QUAS-mNeonGreen::Tm1-A/+; nSyb-QF2/+*			
Supp. Fig. 3D: Pearson's R correlation between Lifeact::Halo and GFP or mNG-Tm1-A.	*C155-Gal4/Y;QUAS-mNeonGreen::Tm1-A/UAS-GFP; nSyb-QF2/+*	7 larvae/20 NMJs		

	C155-Gal4/Y;QUAS-mNeonGreen::Tm1-A/UAS-Lifeact::Halo; nSyb-QF2/+	8 larvae/22 NMJs		
Supp. Fig. 3E-F: Presynaptic localization of QmNGMA-labeled actin assemblies and mNG-Tm1-L is sensitive to treatment with LatA, but not to the vehicle DMSO, supporting F-actin-Tm1 association along the presynaptic actin core.	*C155-Gal4/Y;QUAS-mNeonGreenMA(GMA)/+; nSyb-QF2/+* *C155-Gal4/Y;UAS-Lifeact::Halo/QUAS-mNeonGreenTm1-L; nSyb-QF2/+*	DMSO: 3 larvae/ 9 NMJs LatA: 4 larvae/12 NMJs DMSO: 4 larvae/ 9 NMJs LatA: 4 larvae/ 9 NMJs		
Supp. Fig. 3G: Endogenous Tm1 in larvae expressing control RNAi and *panTm1*^{56869} in neurons.	*C155-Gal4/Y;; UAS-CTRL*^{35785}*/+* *C155-Gal4/Y;; UAS- Tm1*^{56869}*/+*	8 larvae/28 NMJs 7 larvae/14 NMJs	Tm1-A/L fluorescence per µm^2	*** p<0.001 upon one way ANOVA with Kruskal-Wallis multicomparison test. Error bars are SEM.
Supplemental figure 4.	**Supplemental figure 4. Validation of *UAS-RNAi* lines targeting NMII^{HC}/Zip and NMII^{LC}/Sqh.**			
Supp. Fig. 4A-C: Distribution of Sqh::GFP (cyan) in axons (labeled with HRP in magenta) proximal to muscle 4 in Sqh::GFP/+ heterozygous larvae.	*C155-Gal4/Y;; sqh::GFP/+* *C155-Gal4/Y;; sqh::GFP/UAS-Zip*^{65947} *C155-Gal4/Y;; sqh::GFP/UAS-Zip*^{36727} *C155-Gal4/Y;; sqh::GFP/UAS-Sqh*^{32439} *C155-Gal4/Y;; sqh::GFP/UAS-Sqh*^{33892}			
Supp. Fig. 4D: Quantification of Sqh::GFP fluorescence in axons of larvae with the different genotypes shown in the previous panels.	*C155-Gal4/Y;; sqh::GFP/+* *C155-Gal4/Y;; sqh::GFP/UAS-Zip*^{65947} *C155-Gal4/Y;; sqh::GFP/UAS-Zip*^{36727} *C155-Gal4/Y;; sqh::GFP/UAS-Sqh*^{32439} *C155-Gal4/Y;; sqh::GFP/UAS-Sqh*^{33892}	4 larvae/ 16 NMJs 4 larvae/ 8 NMJs 4 larvae/ 8 NMJs 4 larvae/ 16 NMJs 3 larvae/ 6 NMJs	Axonal sqh::GFP fluorescence per µm^2	ns – not significant, *** p<0.001 after One-way ANOVA with Kruskal-Wallis multiple comparison test. Error bars are SEMs.
Supp. Fig. 4E: Example of image analysis in Fiji, where the sqh::GFP fluorescence was measured within the presynaptic terminal (masked by HRP/presynaptic ROI), in a 1 µm rim surrounding the bouton (postsynaptic ROI), and in the muscle ROI (rectangle with yellow dashed lines) (excluding the presynaptic compartment and the 1 um rim surrounding it).	*C155-Gal4/Y;; sqh::GFP/UAS-CTRL*^{35785} *C155-Gal4/Y;; sqh::GFP/UAS-Zip*^{65947} *C155-Gal4/Y;; sqh::GFP/UAS-Zip*^{36727}			

Supp. Fig. 4F: Analysis of the Sqh::GFP fluorescence per µm^2 in muscles of larvae expressing *CTRL-* and *Zip RNAi* lines.	*C155-Gal4/Y;; sqh::GFP/UAS-CTRL^{35785}* *C155-Gal4/Y;; sqh::GFP/UAS-Zip^{65947}* *C155-Gal4/Y;; sqh::GFP/UAS-Zip^{36727}*	10 larvae/ 20 NMJs 7 larvae/ 14 NMJs 7 larvae/ 15 NMJs	Muscle sqh::GFP fluorescence per µm^2	ns – not significant, *** p<0.001 after One-way ANOVA with Kruskal-Wallis multiple comparison test. Error bars are SEMs.
Supp. Fig. 4G-H: Sqh::GFP at NMJs with accompanying quantifications of its presynaptic and postsynaptic Fluorescence, ruling out leaky expression of *Zip^{65947}* in neurons and muscles in absence of Gal4 driver.	*X/Y;; sqh::GFP/UAS-CTRL^{35785}* *C155-Gal4/Y;; sqh::GFP/UAS-CTRL^{35785}* *X/Y;; sqh::GFP/UAS- Zip^{65947}* *C155-Gal4/Y;; sqh::GFP/UAS-Zip^{65947}*	7 larvae/14 NMJs 7 larvae/14 NMJs 5 larvae/10 NMJs 6 larvae/14 NMJs	Presynaptic sqh::GFP fluorescence per µm^2 Postsynaptic sqh::GFP fluorescence per µm^2	ns – not significant, *** p<0.001 after One-way ANOVA with Kruskal-Wallis multiple comparison test.
Supplemental figure 5.	**Supplemental figure 5. Presynaptic actin assemblies are disrupted upon neuronal down-regulation of non-muscle Myosin II.**			
Supp. Fig. 5A: QmNGMA-labeled presynaptic actin in fixed larvae co-expressing CTRL- or NMII/Zip^{65947} RNAi lines.	*C155-Gal4/Y;QUAS-mNeonGreenMA(GMA)/UAS-CTRL^{35785}; nSyb-QF2/+* *C155-Gal4/Y;QUAS-mNeonGreenMA(GMA)/UAS-Zip^{65947}; nSyb-QF2/+*	6 larvae (3 male+3 female)/24 NMJs 6 larvae (3 male+3 female)/20 NMJs		
Supp. Fig. 5B: Quantification of the total actin marker fluorescence, as well as abundance, area, and fluorescence intensity of individual presynaptic actin assemblies	*C155-Gal4/Y;QUAS-mNeonGreenMA(GMA)/UAS-CTRL^{35785}; nSyb-QF2/+* *C155-Gal4/Y;QUAS-mNeonGreenMA(GMA)/UAS-Zip^{65947}; nSyb-QF2/+*	6 larvae (3 male+3 female)/24 NMJs 6 larvae (3 male+3 female)/20 NMJs	Actin fluorescence per µm^2 Number F-actin assemblies per µm^2	ns – not- significant, ** p<0.01, *** p<0.001 upon unpaired, non-parametric Mann-Whitney test. Error bars represent SEMs.
		6 larvae (3 male+3 female)/24 NMJs/2184 6 larvae (3 male+3 female)/20 NMJs/1950	Area of individual presynaptic actin structures (µm^2) Fluorescence of individual presynaptic actin structures	

Supplemental Figure 6.	**Supplemental Figure 6. Neuronal depletion of non-muscle Myosin II and Tm1 rearranges integrin receptors at the NMJ.**			
Supp. Fig. 6A: Pearson's R correlation between Lifeact::Halo and Integrin-β::YFP at NMJs of live larvae.	*C155-Gal4/Y;;UAS-Lifeact::Halo/+;ubiMys::YFP/+*	2 larvae/6 NMJs	Pearson's R correlation	
Supp. Fig. 6B-C: Reorganization of Integrin-β at NMJs of larvae expressing an independent RNAi line *Zip*^{36727} in neurons, compared to controls.	*C155-Gal4/Y;;UAS-CTRL*^{35785}*/+* *C155-Gal4/Y;;UAS- Zip*^{36727}*/+*	10 larvae/20 NMJs 4 larvae /8 NMJs	Fluorescence of presynaptic Integrin-β per μm^2 Fluorescence of postsynaptic Integrin-β per μm^2	Ns – non-significant, *** p<0.001, upon unpaired, non-parametric Mann-Whitney test. Error bars are SEMs.
Supp. Fig. 6D-E: Fluorescence intensity of postsynaptic Integrin-β in presence and absence of *C155-Gal4*.	*X/Y;;UAS-CTRL*^{35785}*/+* *C155-Gal4/Y;;UAS-CTRL*^{35785}*/+* *X/Y;;UAS- Zip*^{65947}*/+* *C155-Gal4/Y;;UAS- Zip*^{65947}*/+*	8 larvae/ 16 NMJs 7 larvae / 14 NMJs 7 larvae/ 14 NMJs 6 larvae / 13 NMJs	Fluorescence of presynaptic Integrin-β per μm^2 Fluorescence of postsynaptic Integrin-β per μm^2	Ns – non-significant, ** p<0.01, *** p<0.001 upon unpaired, non-parametric Mann-Whitney test. Error bars are SEMs.
Supp. Fig. 6F-G: Fluorescence intensity of Integrin-β in myotendinous junctions in control and *Zip*^{65947} larvae.	*C155-Gal4/Y;;UAS-CTRL*^{35785}*/+* *C155-Gal4/Y;;UAS- Zip*^{65947}*/+*	9 larvae/ 18 NMJs 8 larvae / 16 NMJs The myotendinous junctions at muscles 6/7 imaged	Fluorescence of Integrin-β in myotendinous junctions per μm^2	ns – non-significant, upon unpaired, non-parametric Mann-Whitney test. Error bars represent SEMs.